


2016

Cold Gas Dynamic Spray – Characterization of Polymeric Deposition

Trenton Bush

University of Massachusetts - Amherst, tpbush@umass.edu

Follow this and additional works at: http://scholarworks.umass.edu/masters_theses_2

 Part of the [Applied Mechanics Commons](#), [Dynamics and Dynamical Systems Commons](#), [Manufacturing Commons](#), and the [Polymer and Organic Materials Commons](#)

Recommended Citation

Bush, Trenton, "Cold Gas Dynamic Spray – Characterization of Polymeric Deposition" (2016). *Masters Theses May 2014 - current*. 413. http://scholarworks.umass.edu/masters_theses_2/413

This Open Access Thesis is brought to you for free and open access by the Dissertations and Theses at ScholarWorks@UMass Amherst. It has been accepted for inclusion in Masters Theses May 2014 - current by an authorized administrator of ScholarWorks@UMass Amherst. For more information, please contact scholarworks@library.umass.edu.

**COLD GAS DYNAMIC SPRAY – CHARACTERIZATION OF
POLYMERIC DEPOSITION**

A Thesis Presented

by

TRENTON PAUL BUSH

Submitted to the Graduate School of the
University of Massachusetts Amherst in partial fulfillment
of the requirements for the degree of

MASTER OF SCIENCE IN MECHANICAL ENGINEERING

September 2016

Mechanical and Industrial Engineering

© Copyright by Trenton Paul Bush 2016
All Rights Reserved

**COLD GAS DYNAMIC SPRAY – CHARACTERIZATION OF
POLYMERIC DEPOSITION**

A Thesis Presented

by

TRENTON PAUL BUSH

Jonathan P. Rothstein, Co-Chair

David P. Schmidt, Co-Chair

Jae-Hwang Lee, Member

Sundar Krishnamurty, Department Head
Department of Mechanical and Industrial Engineering

ABSTRACT

COLD GAS DYNAMIC SPRAY – CHARACTERIZATION OF POLYMERIC DEPOSITION

SEPTEMBER 2016

TRENTON PAUL BUSH, B.A, GRINNELL COLLEGE

M.S.M.E., UNIVERSITY OF MASSACHUSETTS, AMHERST

Directed by: Professor Jonathan P. Rothstein, Professor David P. Schmidt

When a solid, ductile particle impacts a substrate at sufficient velocity, the resulting heat, pressure, and plastic deformation can produce bonding at the interface. The use of a supersonic gas flow to accelerate such particles is known as Cold Spray deposition. The Cold Spray process has been commercialized for some metallic materials, but further research is required to unlock the exciting material properties possible with polymeric compounds. In this work, a combined computational and experimental study a) simulated and optimized the nozzle flow conditions necessary to produce bonding in a polyethylene particle, b) developed and fabricated an experimental device, and c) explored temperature-pressure space across a range of substrate materials, resolving a material dependent ‘window of deposition’ where successful coatings form. Insights into bonding mechanisms are discussed, and paths forward proposed.

TABLE OF CONTENTS

| | Page |
|---|------|
| ABSTRACT | iv |
| LIST OF TABLES | vii |
| LIST OF FIGURES | viii |
| CHAPTER | |
| 1. INTRODUCTION | 1 |
| 1.1 Cold Gas Dynamic Spray..... | 1 |
| 1.1.1 Comparison to Existing Technologies | 2 |
| 1.2 Gas Dynamics | 3 |
| 1.2.1 Isentropic Flow | 3 |
| 1.2.2 Particle-Gas Interaction | 5 |
| 1.3 Particle-Substrate Interaction..... | 6 |
| 1.3.1 Bonding Mechanism | 7 |
| 1.3.2 Johnson-Cook Working Model..... | 9 |
| 1.3.3 Polymer Studies | 10 |
| 2. METHODS | 12 |
| 2.1 Introduction..... | 12 |
| 2.2 Nozzle Design..... | 12 |
| 2.2.1 One-Dimensional Model..... | 12 |
| 2.2.2 Numerical Optimization..... | 15 |
| 2.2.3 CFD Simulation | 18 |
| 2.2.3.1 Model | 18 |
| 2.2.3.2 Numerical Methods..... | 19 |
| 2.2.4 Setting Nozzle Scale | 23 |
| 2.2.5 Additional Nozzles..... | 24 |
| 2.3 Design and Construction of Experimental Device..... | 26 |

| | | |
|---------|--|----|
| 2.3.1 | Introduction..... | 26 |
| 2.3.2 | Component Selection..... | 26 |
| 2.3.3 | Hopper and Gas System Iterations..... | 28 |
| 2.3.3.1 | Fluidized Bed Hopper..... | 28 |
| 2.3.3.2 | Mechanical Rotating Mesh Hopper..... | 31 |
| 2.3.3.3 | Vibratory Powder Feeder..... | 34 |
| 2.3.3.4 | Linear Spray System..... | 36 |
| 2.3.4 | Material Sourcing..... | 37 |
| 2.3.4.1 | Ball Milling..... | 38 |
| 2.3.4.2 | Cryomilled Powders..... | 39 |
| 2.3.4.3 | Material Selection..... | 40 |
| 2.4 | Experimental Design..... | 40 |
| 2.5 | Analytical Techniques..... | 41 |
| 2.5.1 | SEM..... | 41 |
| 3. | RESULTS AND DISCUSSION..... | 43 |
| 3.1 | Preliminary Materials Testing..... | 43 |
| 3.2 | Like-on-Like Deposition of BYK Ceraflour 916..... | 45 |
| 3.2.1 | Window of Deposition..... | 45 |
| 3.2.1.1 | Measurement Error..... | 46 |
| 3.2.2 | Structural variation..... | 48 |
| 3.2.3 | Numerical Simulation of Particle Trajectory..... | 49 |
| 3.2.4 | Microscopy..... | 51 |
| 3.3 | Variation of Substrate Material..... | 52 |
| 3.3.1 | Windows of Deposition..... | 53 |
| 3.3.1.1 | Adapting the Critical Velocity Model to Polymeric Deposition..... | 54 |
| 3.3.1.2 | Critical Velocity Comparisons..... | 56 |
| 4. | CONCLUSIONS..... | 58 |
| 4.1 | Bonding Mechanism..... | 58 |
| 4.2 | Summary..... | 59 |
| | BIBLIOGRAPHY..... | 61 |

LIST OF TABLES

| Table | Page |
|---|------|
| 2-1. Optimization constraints. | 16 |
| 2-2. Other process parameters and material properties. | 17 |
| 2-3. Optimized Nozzle Geometries | 18 |
| 2-4. ANSYS Fluent properties of air. | 19 |
| 2-5. Actual Nozzle Dimensions. Nozzle “Max Total Energy” was designed to maximize particle total energy, “Max Temp” to maximize particle temperature, “Min Velocity” to explore minimum deposition velocity, and “Max Vel Match” to generate the maximum velocity such that nozzle exit pressure matched atmospheric pressure. | 25 |
| 2-6. Materials and their basic properties. Note: for commercial products, T_g is not given in technical data sheets. The values shown are for generic polymer types. | 39 |
| 3-1. Negative results. These conditions produced a visible roughening of substrate surface, but no deposition. Note: BYK did deposit on Kapton film at elevated temperatures of 50 C. | 44 |
| 3-2. Material and Empirical Fitting Properties. Copper on copper properties are provided for reference. All polymer material properties are from manufacturer data sheets unless otherwise noted. | 55 |

LIST OF FIGURES

| Figure | Page |
|---|------|
| 1-1. Graphical representation of gas properties as a function of axial displacement in a converging-diverging nozzle. (Kaboldy, 2008)..... | 4 |
| 2-1. Diagram of nozzle with design variables L and A/A*..... | 16 |
| 2-2. 67,000 cell mesh of the ‘minimum velocity’ nozzle..... | 20 |
| 2-3. ANSYS Fluent simulation of over-pressured (under-expanded) nozzle. | 22 |
| 2-4. Comparison of Fluent vs 1-D Model for different pressure regimes..... | 23 |
| 2-5. Actual profile of high speed nozzle. | 24 |
| 2-6. Exaggerated profile of actual high-speed nozzle..... | 24 |
| 2-7. Schematic diagram of nozzle geometry. See Table 2-5 for dimensions. Abbreviations correspond to the following: inlet diameter (ID), throat diameter (TD), exit diameter (ED), converging length (CL), constant-area buffer length (CABL), diverging length (DL), and constant-area extension length (CAEL). | 25 |
| 2-8. Branched spray system with fluidized hopper..... | 28 |
| 2-9. Schematic of fluidized powder feed. | 29 |
| 2-10. Photo of pressure vessel flange with attached porous plate..... | 30 |
| 2-11. Schematic of rotating mesh hopper feed system..... | 31 |
| 2-12. Photos of rotating mesh hopper assembly. Shown without (A) and with (B) concentric aluminum hopper insert that contains powder. | 33 |
| 2-13. Photo of 'dots' of deposition resulting from discontinuous powder feed. Sample is BYK Ceraflour 916 sprayed onto LDPE substrate at 25°C and 50 psi..... | 34 |
| 2-14. Schematic of final vibrating hopper design. | 35 |
| 2-15. Schematic of linear spray system..... | 36 |
| 2-16. Photo of linear spray system. Components are: (1) Gas infeed, (2) Process heater, (3) Heated hopper vessel, (4) Nozzle, and (5) Linear stage..... | 37 |

| | | |
|------|---|----|
| 3-1. | Map of lower boundary of deposition for BYK Ceraflour 916 on cast BYK Ceraflour 916 substrate. Filled circles indicate successful deposition, open squares indicate a failure to deposit. The curve is the critical velocity predicted by the working model of Equation 11. (Schmidt, Gärtner, Assadi, & Kreye, 2006) | 45 |
| 3-2. | Morphological variation in like-on-like BYK Ceraflour deposits sprayed at different velocities. Temperature was constant at 24° C. The nozzle traversed right to left during processing. | 48 |
| 3-3. | HDPE particles (46µm diameter) were released just upstream of the nozzle exit with initial velocities equal to the centerline case. The ratio r_0/R represents the fraction of nozzle exit radius R at which the particles were released. A r_0/R value of 0 corresponds to nozzle centerline, and a value of 1 is the nozzle wall. For reference, particle axial velocity was around 240 m/s for the two most central particles, and 180 m/s for the particle closest to the wall. Inlet gas conditions were T = 20° C, P = 72 psi in a 7.21mm long constant-area nozzle. | 50 |
| 3-4. | SEM imaging of like-on-like BYK Ceraflour deposits. Note the lack of discernable particle boundaries. Deposition conditions at impact: 19° C at 197 m/s (left), 17° C at 228 m/s (right)..... | 51 |
| 3-5. | SEM of cross section of deposit. A successful deposit was cut in half with a razor blade and the sheared interface imaged with SEM. Left and right images are different zoom levels of the same sample. At impact, a median diameter (46µm) particle was 19° C with velocity 179 m/s. | 52 |
| 3-6. | Deposition maps of BYK Ceraflour 916 powder on a variety of substrate materials. Closed circles indicate deposition and open squares indicate failure to deposit. The dotted line is a least-squares fit of the working model (equation 11) to the lower deposition boundary (see section 3.3.1.1. ‘Adapting the Critical Velocity Model to Polymeric Deposition’ for details). Boundary points were defined by linear interpolation between the last successful deposit and the first failed deposit points at each temperature. For PVC, POM, and HDPE substrates, room temperature sprays used the converging-diverging to constant-area extension ‘Max Matched-Pressure’ nozzle, and high temperature sprays used the 7.21mm constant area ‘Min velocity’ nozzle. For the cast BYK Ceraflour substrates, the 2 high-velocity points, the 2 points around 40 °C and the low-velocity 22 °C deposit point used the 26.0mm constant-area ‘Max Temperature’ nozzle. All others used the 7.21mm nozzle. | 53 |
| 3-7. | Empirical fit of critical velocity model on four different substrates..... | 55 |

CHAPTER 1

INTRODUCTION

1.1 Cold Gas Dynamic Spray

Coatings empower engineers to decouple the surface properties of a device from the properties of the bulk material underneath. The ability to tune properties such as wettability, corrosion resistance, or electrical conductivity, while maintaining bulk integrity, allows a single device to fulfill multiple roles. This material control often results in more optimal or perhaps entirely novel performance characteristics. A multitude of coating processes exist to enable a multitude of coating applications, but most processes rely on a phase change from vapor, liquid, or solution into the final solid state. For some materials, a phase change disrupts key material properties such as crystalline structure, chemical composition, or nanoparticle distribution, thereby preventing the formation of successful coatings (ARL Center for Cold Spray, 2010). The Cold Gas Dynamic Spray process (CGDS or just cold spray) is an emerging deposition method that is executed entirely in the solid state. This solid state processing expands the range of coatable materials.

In cold spray deposition, a high speed carrier gas accelerates finely divided deposition material through a nozzle. The high velocity particles impact the substrate, where their kinetic energy is converted into plastic deformation energy. The deformation process results in adhesion to the surface. A wide range of materials have been deposited via Cold Spray, including metals, ceramics, composite materials, and polymers, but thorough study has been performed on only a few metallic materials (A. Moridi, 2014).

1.1.1 Comparison to Existing Technologies

The cold spray process is an emerging deposition method in the thermal spray family of technologies. Traditional thermal spray processes like plasma sprays, wire arc, wire flame, detonation guns or high velocity oxy-fuel (HVOF) sprays all involve high temperatures and phase changes. As the name suggests, cold spray deposition occurs at lower temperatures, in fact below the melting point of the coating material. Compared to existing thermal spray technology, the cold spray process offers several key advantages in both the processing itself and in the resulting deposit.

Cold spray processing offers increased flexibility and safety characteristics when compared to thermal spray processes. Flexibility is improved by eliminating the need for extensive surface preparation. For most materials, a simple cleaning is all that is required to spray. In some cases, grit blasting or other surface roughening techniques may improve deposition efficiency, but is not required for deposition. Additionally, operating conditions include standard temperature, pressure, and atmospheric humidity, so a carefully controlled operating environment is unnecessary. In terms of safety, the cold spray process improves on thermal sprays by using only inert process gasses (nitrogen, helium, or sometimes air), rather than combustible oxy-fuel mixtures. The operating environment is also relatively safe; the only other input to the process gas is heat. Unlike competing processes, there is no production of harmful byproducts such as harmful UV radiation, volatile solvent fumes, or noxious combustion exhaust. (ARL Center for Cold Spray, 2010)

Deposit characteristics also differ from thermally sprayed products in several important ways. First and foremost is the solid state bonding process. The absence of liquid or vapor intermediate phases minimizes oxidation, evaporation, and opportunities for

physical or chemical structural alteration. Additionally, solid phase collisions produce a highly dense, compact deposit with low porosity, leave compressive residual stresses, and improve adhesion by mechanically mixing deposit and substrate at the interface. (Champagne & Helfrich, 2014) Finally, with no need to wait for a liquid phase to cool, free standing structures can be built up in a continuous process, meaning that cold spray has considerable potential in additive manufacturing. An overview of gas dynamics is useful before launching into the current understanding of the particle/substrate interaction responsible for successful cold spray deposition.

1.2 Gas Dynamics

In the cold spray process, gas dynamics are responsible for delivering a powder at a desired velocity and temperature. The most crucial element of the gas system is the nozzle. In a properly designed nozzle, a high pressure gas flows into a converging-diverging channel, accelerating to velocity largely determined by the nozzle geometry. The physical basis of this behavior is covered by the study of compressible flow.

1.2.1 Isentropic Flow

In the nozzle, dissipative effects like viscosity and heat transfer occur largely in thin boundary layers near the nozzle walls. This means that much of the gas operates in an adiabatic, reversible regime. Furthermore, in this application, temperatures and pressures are low enough to ignore intermolecular forces and to consider the carrier gas as calorically perfect: the specific heats are approximated as constants. The combination of these three approximations – adiabatic, reversible, and calorically perfect – mean the gas behavior is governed by isentropic flow relation (Equation 1)

$$\frac{p_2}{p_1} = \left(\frac{\rho_2}{\rho_1}\right)^\gamma = \left(\frac{T_2}{T_1}\right)^{\frac{\gamma}{\gamma-1}} \quad (1)$$

Here p is pressure, ρ is density, T is temperature, and γ is the ratio of specific heats.

If the nozzle has low angles of convergence and divergence, an additional approximation can be made: that flow properties vary only with axial displacement. This is known as quasi-one-dimensional flow. Taking a control volume approach and applying conservation equations results in the area-velocity relation in equation 2.

$$\frac{dA}{A} = (M^2 - 1) \frac{du}{u} \quad (2)$$

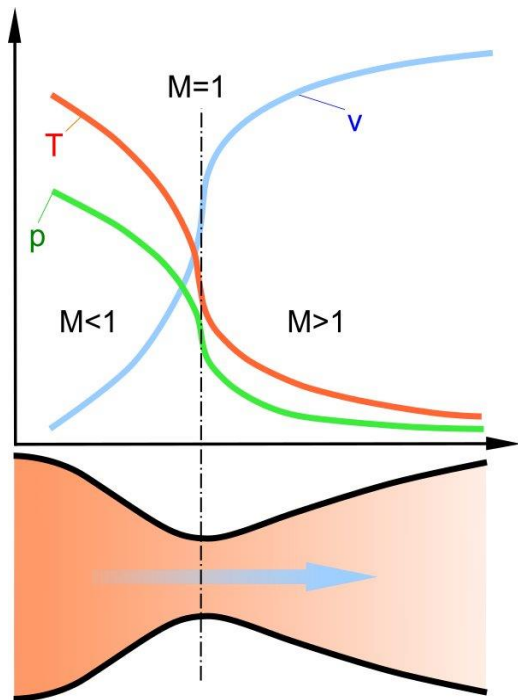


Figure 1-1. Graphical representation of gas properties as a function of axial displacement in a converging-diverging nozzle. (Kaboldy, 2008)

Here A is cross-sectional area, u is velocity, and M is Mach number (see equation 3). Applying equations 1 and 2 to a converging-diverging nozzle yields a series of equations (equations 4-7) relating Mach number, pressure, density, and temperature at any point in the nozzle to the properties at a reference position, usually taken to be the nozzle throat. (Anderson, 2003) An illustration of these isentropic flow relations is given in Figure 1-1.

The principal feature of these relations is that gas velocity increases at the expense of pressure and temperature. This has important

implications for the particle-gas interaction in cold spray.

$$M = \frac{v}{\sqrt{\gamma RT}} \quad (3)$$

$$\frac{A}{A^*} = f(M) = \frac{1}{M} \left[\frac{2 + (\gamma - 1)M^2}{\gamma + 1} \right]^{\frac{\gamma+1}{2(\gamma-1)}} \quad (4)$$

$$\frac{p}{p^*} = \left(1 + \frac{\gamma - 1}{2} M^2 \right)^{-\frac{\gamma}{\gamma-1}} \quad (5)$$

$$\frac{T}{T^*} = \left(1 + \frac{\gamma - 1}{2} M^2 \right)^{-1} \quad (6)$$

$$\frac{\rho}{\rho^*} = \left(1 + \frac{\gamma - 1}{2} M^2 \right)^{-\frac{1}{\gamma-1}} \quad (7)$$

Here superscript * indicates sonic conditions (at the throat).

1.2.2 Particle-Gas Interaction

The inverse relationship between velocity and temperature of the carrier gas necessarily carries over to the entrained particles. The faster a particle is accelerated, the colder the particle will be.

Additional gas dynamic effects arise from particle interaction with shocks as the gas decelerates between the nozzle exit and the substrate. Bow shocks in particular can significantly slow particles and harm deposition efficiency. Such losses can be mitigated by lengthening the standoff distance between nozzle and substrate, allowing turbulent mixing with entrained gas to decelerate the free jet to subsonic velocity (Pattison, Celotto, Khan, & O'Neill, 2008)

Another approach to the bow shock issue is to use a diffuser to decelerate the carrier gas below Mach 1 before it exits the nozzle. Such a solution is only viable for low velocity sprays, such as for polymers. (Alhulaifi, Buck, & Arbegast, 2012)

Finally, studies have also shown the limits of high aspect ratio nozzles, in which viscous losses eventually siphon enough energy from the gas to induce a shock. (Yin, Zhang, Guo, Liao, & Wang, 2013) (A. P. Alkhimov, 2001) In the case of a polymer deposit, it is possible that this may be used as a feature to minimize the bow shock effect.

1.3 Particle-Substrate Interaction

Cold spray deposition relies on an interaction between a high velocity particle and a substrate to create bonding. Over the past 15 years, researchers around the world have studied this process, looking for insight into successful deposition. Much of the literature has, in general, a focus on applied solutions, and the vast majority of cold spray research has gone into sprays of metallic material such as aluminum and titanium. Studies of gas dynamics are of universal interest, but many papers have been published related to, for example, the most efficient deposition conditions for 6061-T6 aluminum or the temperature that produces the highest electrical conductivity in copper. While useful for industry, it is often difficult to generalize such results into an understanding of cold spray for polymeric material. Sometimes, however, a study is concerned with more fundamental physics of particle/substrate deformation. It is in these studies that metals and polymers can hope to find common ground.

1.3.1 Bonding Mechanism

Understanding the mechanics of deposition is key to the design of processing conditions. For metal deposition, various ideas for bonding mechanisms have been proposed and examined over the past 15 years. Assadi et al. were the first to discover a necessary criterion for deposition: during particle impact, plastic strain energy is released locally as heat, which softens the material and encourages further deformation and heat release. (Assadi, Gärtner, Stoltenhoff, & Kreye, 2003) This positive feedback condition, termed the adiabatic shear instability, occurs at high strain rates where the rate of thermal softening exceeds the rates of strain and strain-rate hardening. Assadi et al. proposed that the extensive deformation and heating at the interface disrupted oxide layers and allowed the formation of metallic bonds between particles and substrate. The authors noted, however, that the adiabatic shear criterion was a necessary but not sufficient condition for deposition: “if the contact time is too short, or the applied tensile stress at the interface is too high, a particle may bounce back before the conditions for bonding are achieved.”

Most studies have provided support for mechanisms based on either topochemical reactions or mechanical interlocking. But no single mechanism is capable of explaining all experimental results, due to the sheer diversity of material combinations and corresponding physics involved. For example, surface chemistry plays a particularly dominant role in the deposition of reactive metals such as titanium and its alloys. Li et al. showed that Ti-6Al-4V particles reacted with entrained oxygen in the area between nozzle exit and substrate, despite the use of helium or nitrogen as a process gas. These reactions generated enough heat to successfully deposit Ti-6Al-4V even at low impact velocities that produced almost no deformation of the particles. (W.-Y. Li C. Z.-T.-J., 2007) In a later

paper, Li et al. conclude that most metals possibly experience local melting at interfaces, benefitting the formation of metallic bonds across the interface. The authors suggest that the methods or properties that result in local melting differ across materials: low melting point, high gas temperature, atmospheric reactions, or poor thermal conductivity could play a role in the production of local melting. (W.-Y. Li C. Z.-J., 2007)

Klinkov et al. noted that a mechanical mixing mechanism could not account for successful coatings on brittle glass and ceramic substrates, and a mechanism based on simultaneous impacts was statistically unlikely and did not match observed deposition efficiencies. They concluded that the mechanism of topochemical reactions held the greatest explanatory value due to its ability to account for size and velocity dependence of deposition efficiency and for the existence of an ‘incubation time’ during which the substrate surface is activated by impinging particles. (Klinkov, Kosarev, & Rein, 2005)

In a novel proposition, Hussain et al. suggested a combined mechanism based on a modified composite strength model, with one fraction of interfacial area joined by metallurgical bonding and another fraction by mechanical interlocking. In this model, adhesion failure of the coating must be a result of failures in both regions. By using surface preparations to vary the ratio of metallic bonding to mechanical interlocking, the authors reported that mechanical interlocking was able to account for a large proportion of the total bond strength. For their experiments (copper on aluminum alloy), metallic bonding dominated only on a polished and annealed surface where the fraction of metallic bonding approached 100%. (Hussain T. M., 2009) For an extensive review of many proposed bonding mechanisms, see Hussain. (Hussain T. , 2013)

1.3.2 Johnson-Cook Working Model

Another landmark paper in the cold spray world was the creation of a semi-empirical model of the critical velocity. (Schmidt, Gärtner, Assadi, & Kreye, 2006) The model was developed by combining two separate semi-empirical models of impact physics. First they developed a model based on plastic deformation at the interface:

$$F_1 \cdot \sigma \cdot \left(1 - \frac{T_p - T_{ref}}{T_m - T_{ref}}\right) = \frac{1}{8} \rho_p \cdot v_{crit}^2 \quad (8)$$

Here F_1 is an empirical fitting constant, T_m is particle melt temperature, T_p is particle temperature at impact, T_{ref} is the temperature at which particle material properties were measured, σ is particle tensile strength, ρ_p is particle density. The left hand term is an empirical fit on tensile strength modified by the Johnson-Cook model of thermal softening. The right hand term is a ballistic model of the pressure felt by the leading face of a sphere during impact. The second model was a simple energy balance against the melting point of the particle:

$$F_2 \cdot c_p \cdot (T_m - T_p) = \frac{1}{2} \cdot v_{crit}^2 \quad (9)$$

Here c_p is specific heat and F_2 is another fitting constant.

Schmidt et al. then weight each model by 0.5, combine the two, and solve for velocity:

$$v_{cr} = \sqrt{F_2 \cdot c_p (T_m - T_p) + F_1 \cdot \frac{4\sigma}{\rho_p} \left(\frac{T_m - T_p}{T_m - T_{ref}}\right)} \quad (10)$$

The authors note that the combined model “matches better with experimental results than [either individual model] on their own.”

In recent years, the most common form of the equation has had the smaller of the two fitting constants factored out into a single leading constant, giving critical velocity model that has guided the cold spray industry for a decade:

$$v_{cr} = k \sqrt{c_p(T_m - T_p) + \frac{16\sigma}{\rho_p} \left(\frac{T_m - T_p}{T_m - 293} \right)} \quad (11)$$

Here k = fitting constant dependent on particle size, c_p = specific heat, T_m = particle melt temperature, T_p = particle temperature at impact, σ = particle tensile strength, ρ_p = particle density. (Schmidt, Gärtner, Assadi, & Kreye, 2006) The extra factor of 4 in the mechanical model is a remnant of the separate fitting constants; for metals, the thermal constant had a value of 0.3 and a mechanical constant of 1.2. Factoring out 0.3 leaves the factor of 4 behind. The model in equation 11 is the dominant critical velocity model used today, and was used as the working model for this study.

1.3.3 Polymer Studies

Only a handful of papers directly involve polymer deposition. In 2006, Xu and Hutchings demonstrated deposition with large 150 and 250 micron HDPE particles. They observed a critical velocity around 100 m/s, with very low deposition efficiency (<0.6%). Deposition was possible on polyethylene substrates, but depositing on aluminum required the use of a prepared bonding layer of HDPE. They also noted that deposition efficiency increased linearly with feed rate. (Xu & Hutchings, 2006)

Researchers at the South Dakota School of Mines used a nozzle with a diffuser, discussed earlier, to deposit HDPE directly on an aluminum substrate. Particles were sieved

to 53-75 microns, and they observed a critical velocity of 191 m/s. (Alhulaifi, Buck, & Arbegast, 2012)

Finally, Ganesan et al. sprayed copper and tin powders onto PVC and epoxy substrates. They noted that of their two copper powders, one spherical and the other dendritic, the dendritic powder bonded more readily with the soft polymer substrates, but struggled to build up once the particles were impacting only copper. Their most successful method was to spray down a thin interfacial layer of dendritic copper before switching to spherical powder to build thickness. (Ganesan, Yamada, & Fukumoto, 2013) This demonstrates an interesting solution to spraying materials with mis-matched hardness.

CHAPTER 2

METHODS

2.1 Introduction

In order to study cold spray deposition of polymeric material, a complete spray system was designed and built from scratch. Armed with the working model from the literature, the design process began with the spray nozzle and propagated backwards to the hopper and gas supply. Considerable effort was expended on the experimental apparatus, particularly the powder feed hopper. Over the course of development, preliminary data were collected over a range of spray conditions and materials, eventually leading to the current study.

2.2 Nozzle Design

In the cold spray process, the carrier gas system is merely a tool to enable the particle-substrate impact responsible for deposition. As discussed previously, the core of the gas system is the particle-gas interaction in the nozzle. The nozzle must provide acceleration sufficient to reach the critical velocity, but cannot rob the particles of so much heat that they excessively harden. Several computational models were used to design such nozzles. In the interests of brevity, the design process presented here is more linear than it was in reality.

2.2.1 One-Dimensional Model

The first model was a quasi-1-D simulation provided by Dr. Dennis Helfrich of Army Research Laboratory. (Champagne V. K., 2011) In this model, the gas dynamics of

the de Laval nozzle were approximated with 1-D isentropic flow equations, then particle properties were subsequently calculated with a first order scheme.

To determine the gas dynamics with isentropic flow equations, a spatial discretization was not useful because the area ratio expression $A/A^* = f(M)$ (equation 4) cannot be inverted in closed form. Therefore, a discretization was performed over M and used to calculate the local area ratio, pressure, density, and temperature from the flow equations. Spatial coordinates were calculated from the area ratio and input nozzle geometry.

Particle velocity was determined by a drag force from the carrier gas. The velocity of a spherical particle can be calculated from the following force balance: (Assadi, et al., 2011)

$$v_p \frac{dv_p}{dx} = \frac{3}{4} C_d \frac{\rho_{gas}(v_{gas} - v_p)|v_{gas} - v_p|}{\rho_p d_p} \quad (12)$$

Here x is axial distance along the nozzle, d_p is particle diameter, and C_d is a drag coefficient. The drag coefficient on the particle is dependent on the relative Mach number of the particle, given by equation 13. (Walsh, 1975)

$$C_d = \frac{\left(\frac{24}{R_e}\right) \left((1 + 0.15(R_e^{0.687})) \left(1 + e^{-\frac{0.427}{M_p^{4.63}} \frac{3}{R_e^{0.88}}} \right) \right)}{1 + \left(\frac{M_p}{R_e}\right) \left(3.82 + 1.28e^{-\frac{1.25R_e}{M_p}} \right)} \quad (13)$$

Here M_p = particle Mach number and R_e = Reynold's number. This drag coefficient was modified by a shape factor that ranges from 1.0 for a sphere to 1.88 for platelets (like talc). Because shape factor was an unknown empirical quantity at this stage, and the heat transfer model assumes sphericity, the shape factor was set to the spherical value of 1.0.

For heat transfer, semi-empirical relations for viscosity (via Sutherland's formula) and conductivity (Goharshadi, 2009) were used to calculate Reynolds and Prandtl numbers, from which Nusselt number was calculated via the spherical correlation:

$$Nu = 2 + Re^{\frac{1}{2}} \cdot Pr^{\frac{1}{3}} \quad (14)$$

Once a Nusselt number was obtained, heat transfer was modeled as a lumped capacitance using a spatial discretization:

$$\Delta T = \frac{6 \cdot Nu \cdot k \cdot (T_{gas} - T_{particle}) \cdot \left(\frac{\Delta x}{v_{particle}}\right)}{(C_p \cdot \rho \cdot d_p^2)} \quad (15)$$

Here k is gas conductivity.

The result of all this computation is a tool that takes inputs of particle material properties (size, density, heat capacity, ultimate stress, melt point, and shape), nozzle geometry, and gas stagnation temperature and pressure, and outputs particle velocity and temperature along the flight path to impact.

A limitation of this method is the assumption behind the simulated particle temperature. Temperature is modeled as a lumped capacitance, meaning that spatial variation of temperature within the particle is neglected. For metals, that is a reasonable assumption, due to high thermal conductivity and small particle size. The HDPE particles used in this study, however, are both worse thermal conductors and much larger. The validity of the lumped capacitance model can be evaluated with the Biot number.

The Biot number is a dimensionless ratio of convective heat transfer into the particle to conductive heat transfer within the particle.

$$Bi = \frac{hL_c}{k_b} \quad (16)$$

Here h is the convective heat transfer coefficient, L_C is a characteristic length, and k_b is thermal conductivity of the body. A Biot number less than 0.1 is generally considered the cutoff point of for a lumped capacitance model. Biot number was calculated by modifying the Nusselt number empirical formula above.

Both Biot number and Nusselt number involve a ratio of convective heat transfer to conductive heat transfer, but the Biot number considers conduction in the particle, while Nusselt considers conduction in the fluid. To convert between the two, I simply multiplied by the thermal conductivity ratio of particle to gas, or vice versa.

Biot number was calculated along the particle flight path, and ranged from 0.4 at the nozzle inlet to over 3 in the fast, cold gas flow of the diverging portion of the nozzle. This is a violation of the lumped capacitance assumption.

The error resulting from this modeling inaccuracy is that the surface temperature of the particles will be colder than predicted. This cold ‘jacket’ around the particles will result in less total heat loss from the particle, so the interior will be warmer than predicted. In the context of the adiabatic shear instability mechanism, however, interface temperature is most important, so we would expect actual deposition to be worse than simulations suggest. FEA is best suited to answer questions about the degree to which thermal gradients effect plastic deformability.

2.2.2 Numerical Optimization

The Johnson-Cook critical velocity model states that particle temperature and particle velocity are substitutes for each other. This implied that a critical velocity could be met by one of two alternate strategies. The first strategy was to maximize particle temperature, which, according to the working model of deposition, would substantially

soften the particle and require only a low particle velocity to deposit. The second strategy was the brute force method; to maximize particle velocity and overcome the high critical velocity requirements of a cold particle. The high velocity strategy, however, demands much more from the gas system (high pressure, high temperature, high flow rate), so a compromise was used instead. The second strategy actually used in nozzle design was to maximize total particle energy (defined as kinetic plus thermal), subject to the constraints of the experimental setup.

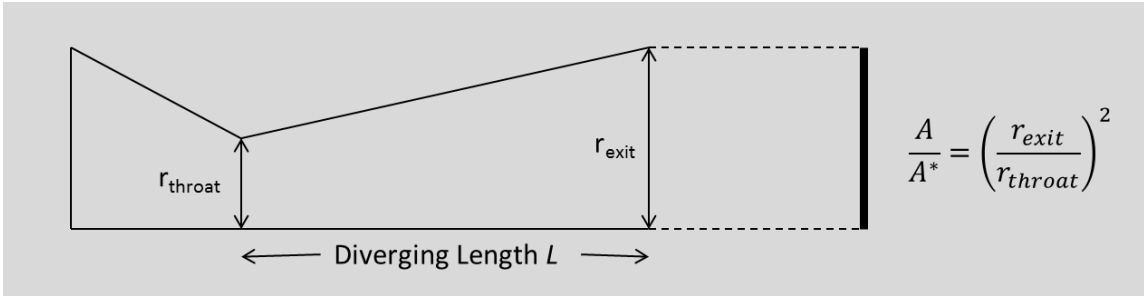


Figure 2-1. Diagram of nozzle with design variables L and A/A^* .

Numerical optimization was performed by maximizing temperature or total energy via a Generalized Reduced Gradient (GRG) method. The parameters varied were area ratio and length of the diverging section. Table 2-1 shows the constraints used.

Table 2-1. Optimization constraints.

| | | |
|--------------------------------|--|------|
| Diverging Angle $\leq 8^\circ$ | $g_1(x) = \left(\frac{180}{\pi}\right) \tan^{-1}\left(\frac{r_{exit} - r^*}{L}\right) - 8$ | (17) |
| Critical Condition | $g_2(x) = v_{cr} - v_{pi}$ | (18) |
| Length constraint | $0.005\text{m} \leq L \leq 0.1\text{m}$ | (19) |
| Area Ratio constraint | $1.001 \leq \frac{A}{A^*} \leq 8$ | (20) |

The diverging angle constraint was a conservative limit on the rate a supersonic gas can expand without separating from the nozzle walls. The side constraint on length was a manufacturing consideration; machining 1.6mm holes longer than 10cm is difficult. The lower bound on area ratio was present simply because the model cannot account for subsonic flow. The upper bound was a consideration of maximum volume flow rate of gas for current instrumentation, but was later recognized to be incorrect. Luckily, that erroneous constraint was not active for the solutions produced, and did not impact the results.

Additionally, the following material and process constants were used:

Table 2-2. Other process parameters and material properties.

| | |
|---|----------------|
| Carrier Gas | N ₂ |
| Polymer material | HDPE |
| T ₀ | 130 C |
| Standoff Distance (nozzle to substrate) | 0.02 m |
| Converging Length | 0.01 m |
| Material (HDPE) Properties | |
| Particle diameter | 46μm |
| Melting point | 135 C |
| Ultimate Stress | 25 MPa |
| C _p | 2250 J/kg-K |
| Enthalpy of Fusion | 245000 J/kg |
| Thermal Conductivity | 0.49 W/(mK) |

The resulting nozzle geometries are presented in Table 2-3.

Table 2-3. Optimized Nozzle Geometries

| Geometry | Max Total Energy Nozzle | Max Temperature Nozzle |
|------------------------|-------------------------|------------------------|
| Converging Length (cm) | 1.00 | 1.00 |
| Diverging Length (cm) | 3.35 | 0.50 |
| Area Ratio | 3.868 | 1.001 |
| Standoff (cm) | 2.00 | 1.00 |

Before machining nozzles based on the 1-D calculations, the results were validated using the ANSYS Fluent 14.5 computational fluid dynamics (CFD) package.

2.2.3 CFD Simulation

2.2.3.1 Model

To model supersonic flow in a nozzle, the governing equations then must allow for compressibility. In order to couple flow velocity to static temperature, the energy equation (equation 21) is enabled:

$$\begin{aligned} \frac{\partial}{\partial t}(\rho E) + \nabla \cdot (\vec{v}(\rho E + p)) \\ = \nabla \cdot \left(k_{eff} \nabla T - \sum_j h_j \vec{J}_j + (\vec{\tau}_{eff} \cdot \vec{v}) \right) + S_h \end{aligned} \quad (21)$$

Where k_{eff} is the effective conductivity $k + k_t$, k_t is the turbulent thermal conductivity, and \vec{J}_j is the diffusion flux of species j . In this application, only one species is present.

An equation of state is necessary to fully determine the system of equations, and here air is modeled as a perfect gas with properties seen in Table 2-4.

Table 2-4. ANSYS Fluent properties of air.

| Physical Properties of Air | |
|---------------------------------------|-------------------------|
| Specific Heat, C_p (j/kg-K) | 1006.43 |
| Thermal conductivity, k (w/m-K) | .0242 |
| Viscosity, μ (kg/m-s) | 1.7894×10^{-5} |
| Sutherland's Law Coefficients | |
| Reference Viscosity, μ_o (kg/m-s) | 1.716×10^{-5} |
| Reference Temperature, T_0 (K) | 273.11 |
| Effective Temperature, S (K) | 110.56 |

In the diverging portion of the nozzle, the Reynolds Number reaches values of order 10^6 , necessitating a turbulence model. In the interests of efficiency, I opted for a RANS k- ϵ RNG model. According to the FLOTRAN Fluids Analysis Guide, the Standard k- ϵ Model often over-predicts the amount of turbulence in regions undergoing significant normal strain (such as a converging nozzle), and the resulting effective viscosity may interfere with shock modelling. (ANSYS Academic Research) The RNG variant is more robust in regions of large strain, hence its selection.

For one particular nozzle type with a long, constant-area section located after a converging-diverging geometry, the Fanno flow conditions resulted in a solution that was very sensitive to viscosity. In this case, the three-coefficient expression of Sutherland's Law was used to model the temperature dependence of viscosity.

2.2.3.2 Numerical Methods

Meshing strategy was determined by the geometry of the nozzle and anticipated flow characteristics. The rotational symmetry of the nozzle made it a logical candidate for

an axisymmetric, 2-D mesh. High density mesh was used in areas of high gradients: within the nozzle, in the exit stream, and at the substrate. Inlet regions and the exit domain were less dense. Figure 2-2 shows an example mesh for the ‘minimum velocity’ nozzle (see section 2.2.5 Additional Nozzles).

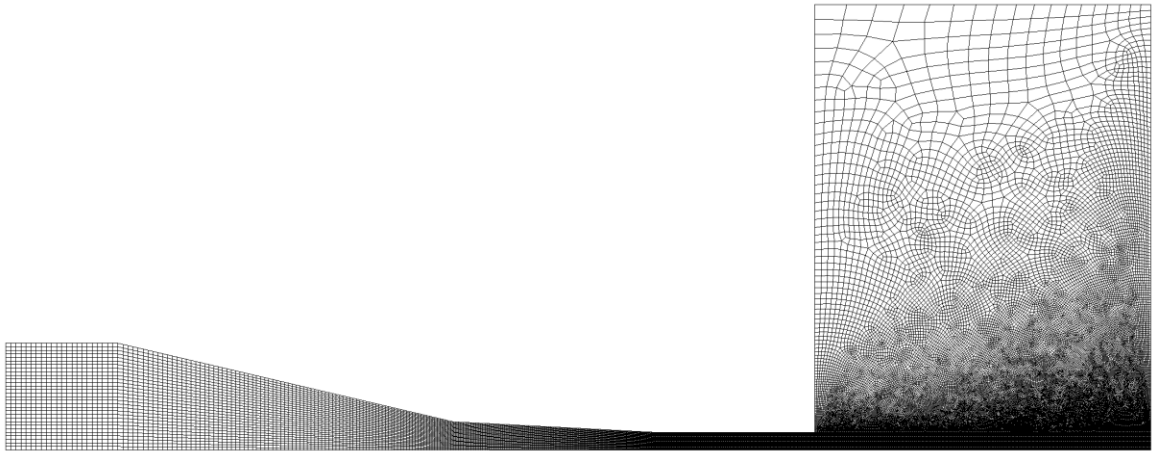


Figure 2-2. 67,000 cell mesh of the ‘minimum velocity’ nozzle.

The exit domain was designed to be large enough (20 times the outlet radius) to sufficiently isolate the outlet boundary from the jet, allowing an imposed boundary condition of atmospheric pressure and room temperature (300K). The inlet boundary was placed upstream of the converging portion of the nozzle (~2.5 times the inlet radius) to allow flow properties, especially turbulence, to develop before reaching the nozzle.

ANSYS Fluent offers two different solvers: pressure-based and density-based. Both methods use the momentum equations to obtain the velocity field. The density-based method uses the continuity equation to obtain the density field, and determines pressure from the equation of state. The density based solver was originally designed with high Mach number flows in mind and offers superior shock resolution, making it the logical choice here. (ANSYS Academic Research)

The density-based solver offers a fully implicit formulation. The speed and stability advantages of the implicit form come at a cost of memory, but this simulation was small enough to neglect that cost. The flux scheme selected was Advanced Upstream Splitting Method (AUSM). This flux-vector splitting scheme first computes a cell interface Mach number based on characteristic speeds from neighboring cells. The interface Mach number is then used to determine the upwind extrapolation for the convection part of the inviscid fluxes. A separate Mach number splitting is used to determine the pressure terms. The AUSM scheme offers exact resolution of shock discontinuities, preserves positivity of scalar quantities, and is free of oscillations at shock fronts. (ANSYS Academic Research) This scheme is ideal for compressible flow.

The default gradient method, Least Squares Cell-based, was used. The motivation for this study was the design of process conditions, so a steady-state solution was selected.

As a general prescription, flow properties were advected with first order upwinding at first, until the solution was stable enough to switch to 2nd order upwinding. Some cases never reached the 2nd order stability region, and others never converged even with 1st order upwinding. The most notable failure in this regard was with a proposed diffuser nozzle, in which a second throat would decelerate and heat the carrier gas after the particles had been brought up to speed. For all nozzle cases, a significant source of error was where the supersonic jet encountered stagnant gas. For under-expanded and matched pressure nozzles, this error occurred where the jet exited the nozzle. For over-expanded nozzles, this error occurred where the normal shock induced boundary layer separation.

This CFD validation process revealed an important limitation of the 1-D model. By assuming 1-D flow, the model cannot account for the multi-dimensional phenomenon

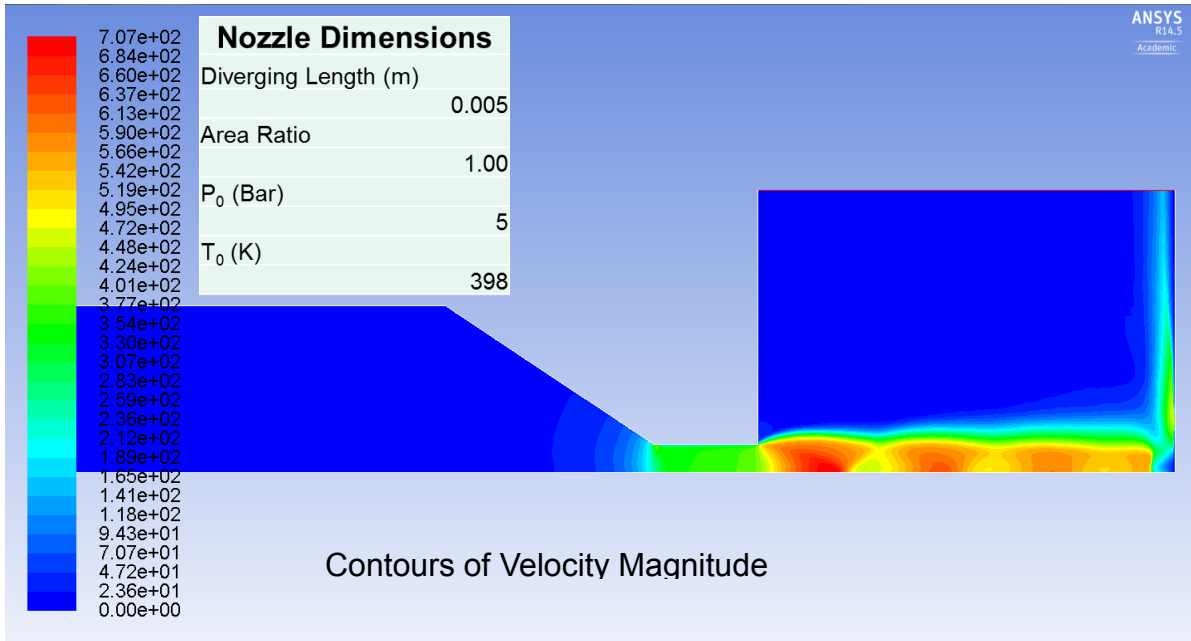


Figure 2-3. ANSYS Fluent simulation of over-pressured (under-expanded) nozzle. of over- or under-expanded gas. In the Fluent solution for the maximum temperature nozzle seen in Figure 2-3 , mismatched pressures at the nozzle exit from under-expansion of the gas result in re-acceleration in the standoff region between the nozzle and the substrate, leading to much higher velocities than the 1-D model, as seen in the first plot of Figure 2-4. The second plot of Figure 2-4 shows a comparison with an appropriately pressured model. When pressures were matched, the 1-D solution gave 3-4% higher velocities, likely due to the lack of viscous and turbulent effects that are included in the Fluent model.

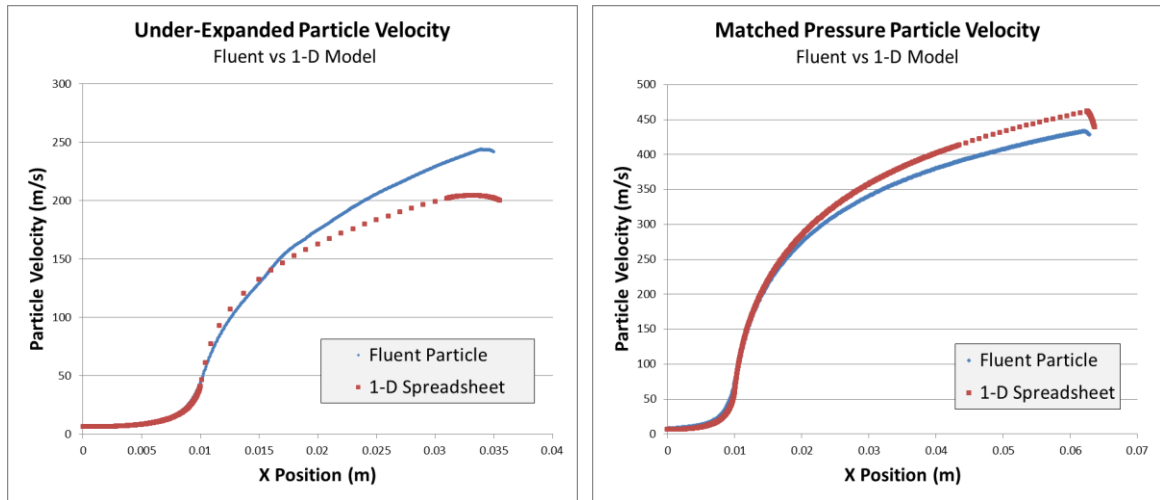


Figure 2-4. Comparison of Fluent vs 1-D Model for different pressure regimes

2.2.4 Setting Nozzle Scale

An iterative design process adapted the proposed nozzles from 1-D and CFD simulations to the nozzles actually produced. The first lesson from the 1-D model was that a nozzle had to be sized down to the research scale. The nozzle profiles from the literature were designed for commercial use and would empty a standard 340 cubic foot nitrogen gas cylinder in less than 10 minutes. By reducing throat diameter from 2.7mm to 1.6mm (1/16”), throat area (and thus volume flow rate) was reduced by a factor of 2.85. Second, the lower material strength of polymers compared to metals meant that high velocities of 500+ m/s and their requisite pressures of 20-30 bar (300 - 450 psi) were deemed unnecessary. A reduction in gas stagnation pressure allowed the scaled-down nozzles to operate on a consumer grade air compressor at 90 psi and 3 SCFM.

Machining concerns also played a role in nozzle design. The scaled down nozzles were too small to produce via CNC milling, and had to be made by hand. But the prescribed diverging length of the high speed (maximum total energy) nozzle meant that the diverging angle was 1.4°; a strange angle that had no obvious tooling. The nearest achievable angle

was 3°, which necessitated a re-optimization of length. The final, physical nozzle dimensions are given in Figure 2-5.

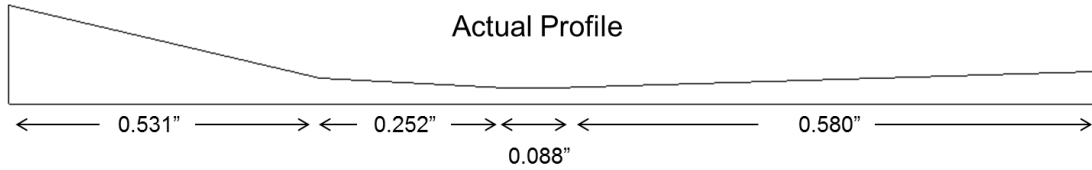


Figure 2-5. Actual profile of high speed nozzle.

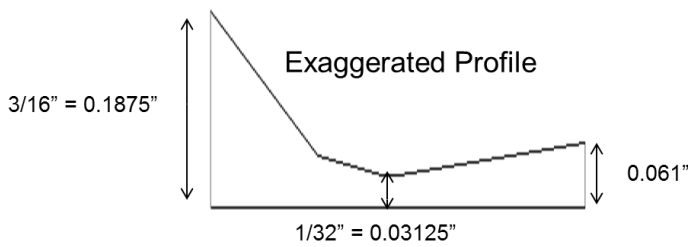


Figure 2-6. Exaggerated profile of actual high-speed nozzle.

The designed precision of the model is to 1 mil. This precision was chosen to reflect the ideal tolerances of milling an actual nozzle.

2.2.5 Additional Nozzles

Two additional nozzles were later designed to explore the upper and lower limits of velocity given the existing compression capabilities. These are seen in Table 2-5. The minimum velocity nozzle was designed to fit interchangeable lengths of 1/16" ID hypodermic tubing. The most used length was 7.21mm. The "Max Vel Match" nozzle was designed to maximize particle velocity with two key constraints: 1) the ceiling of compressor pressure at 72psi, and 2) static pressure at the nozzle exit equal to atmospheric pressure (to minimize shock phenomena at nozzle exit). The design principle was to use a

standard converging-diverging nozzle, expand the gas until the atmospheric pressure constraint was reached, then channel the weakly-supersonic gas stream through a constant-area extension to maximize particle residence time and thus velocity.

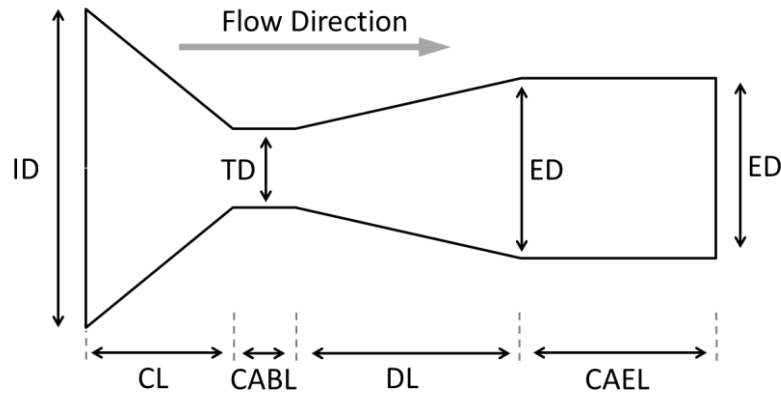


Figure 2-7. Schematic diagram of nozzle geometry. See Table 2-5 for dimensions. Abbreviations correspond to the following: inlet diameter (ID), throat diameter (TD), exit diameter (ED), converging length (CL), constant-area buffer length (CABL), diverging length (DL), and constant-area extension length (CAEL).

Table 2-5. Actual Nozzle Dimensions. Nozzle “Max Total Energy” was designed to maximize particle total energy, “Max Temp” to maximize particle temperature, “Min Velocity” to explore minimum deposition velocity, and “Max Vel Match” to generate the maximum velocity such that nozzle exit pressure matched atmospheric pressure.

| Geometry | Max Total Energy | Max Temp | Min Velocity | Max Vel Match |
|-------------------------------------|-------------------------|-----------------|---------------------|----------------------|
| Inlet Diameter [cm] | 0.952 | 0.952 | 0.952 | 0.952 |
| Throat Diameter [cm] | 0.159 | 0.159 | 0.159 | 0.159 |
| Exit Diameter [cm] | 0.310 | 0.159 | 0.159 | 0.190 |
| Converging Length [cm] | 2.21 | 2.39 | 2.31 | 2.99 |
| Constant-Area Buffer Length [cm] | 0.223 | N/A | N/A | 0.069 |
| Diverging Length [cm] | 1.47 | 2.60 | 0.721 | 0.297 |
| Constant-Area Extension Length [cm] | N/A | N/A | N/A | 4.185 |
| Area Ratio | 3.81 | 1.00 | 1.00 | 1.45 |

The constant-area buffer section (see Figure 2-7) was purely a manufacturing consideration: overlap of opposing cones for the converging and diverging sections would enlarge the nozzle throat. The constant-area buffer is a short, straight length that prevents such overlap and preserves throat diameter.

2.3 Design and Construction of Experimental Device

2.3.1 Introduction

Constructing the spray apparatus was an iterative process that took many months. The first steps were to select supply components that matched the nozzle scale and input requirements. Then, powder feed design took precedence. Finally, powder sourcing issues were overcome and preliminary tests could commence.

2.3.2 Component Selection

With the two nozzle prototypes machined, the flow rate of carrier gas was almost set, only subject to pressure variation. The components were mostly selected to withstand a pressure of 200 psi, where possible. A 2.5 horsepower compressor was adequate to supply continuous feed of 5 CFM at 90 psi. This exceeded the nozzle draw of approximately 3 CFM. At that flow rate, the heating power necessary to reach 200°C was about 550 watts, so an 800 watt in-line process heater was installed. The process heater was only rated to 90 psi, because high pressure immersion heaters were outside the budget. Tubing diameter was selected based on flow velocity; gas flow had to be fast enough to entrain powder. A 3/8" tube would convey the gas at approximately 2 m/s, which seemed sufficient. This was enough velocity to convey the Spherglass powder used in initial testing, but would later prove insufficient for some cohesive polymers. Finally, heat losses over the tubing length

necessitated the installation of ½” fiberglass insulation, which was then wrapped in aluminum foil.

On the instrumentation side, temperature and pressure monitoring are the primary concern. An Omega PX309-300GV pressure transducer monitors nozzle inlet pressure up to 300 psi. The accuracy of the transducer is $\pm 0.25\%$, but the supporting electronics, specifically the 8-bit LCD display, limit resolution to $300/256 = 1.17$ psi. (Omega Engineering Inc, 2014) In practice, the display often oscillates between two values, making effective resolution only 2 psi.

Temperature is measured in three places in the system: at the hopper, at the nozzle inlet, and at the outlet of the heater. A PID temperature controller regulates hopper temperature by switching three 500 watt band heaters on and off. Temperature often overshoots by as much as 10 degrees past the set point, particularly on the first warm up cycle, but the thermal inertia of the hopper is high enough to complete an experiment before the temperature drifts away. The nozzle inlet and heater outlet are monitored manually with a thermocouple reader. At first, a PID controller was also used to control gas temperature, but the relay switching mechanism was orders of magnitude too slow to produce a continuous gas temperature. A PWM output may have worked, but the controller did not have that capability. Instead, an autotransformer was used to manually control heating power. A calibration curve was made to roughly adjust temperature, with fine adjustment performed manually. With the current compressor and heater, carrier gas temperature is controllable from room temperature to over 270°C.

Travel speed is determined from the substrate side rather than at the nozzle. The substrate is placed on a linear stage controlled by a DC motor. Travel speed is controlled

by adjusting input voltage to the motor using a variable power supply. Maximum stage displacement is 146 mm, at speeds from 1.5 to 19.6 mm/s.

2.3.3 Hopper and Gas System Iterations

The first spray system designs revolved around a fluidized bed hopper design. The system design was built to emphasize particle preheating – if the particles entered the nozzle just below their melting point, they would still be soft by the time they impacted the substrate. As seen in Figure 2-8, the gas stream is heated prior to passing through the fluidized hopper.

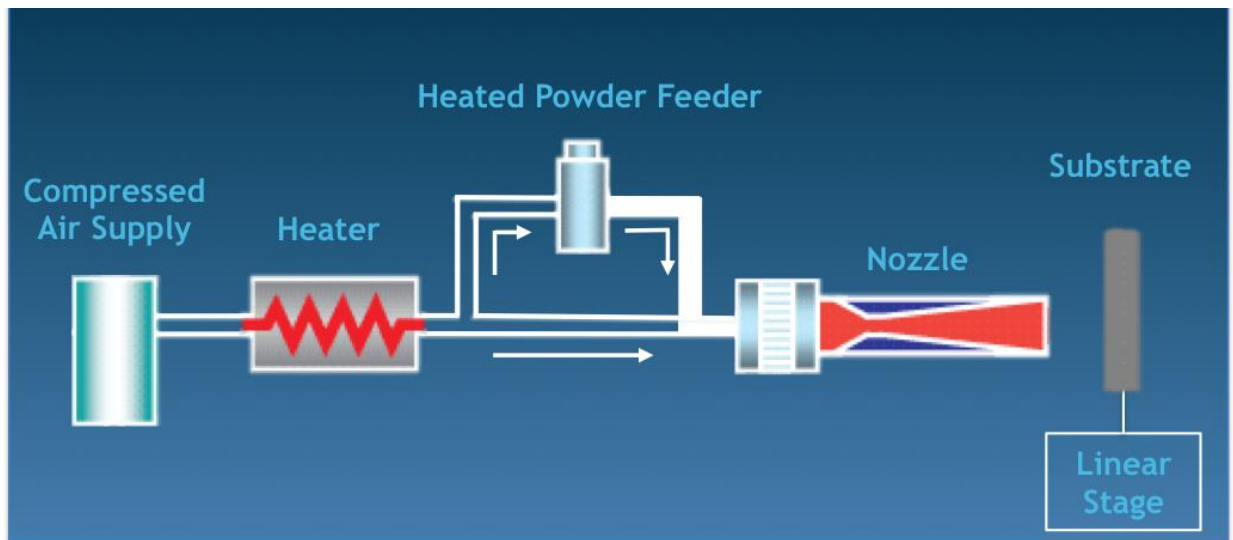


Figure 2-8. Branched spray system with fluidized hopper.

2.3.3.1 Fluidized Bed Hopper

The fluidized bed hopper design was inspired by powder feeds used in electrostatic spray coating, and can be seen in Figure 2-9. Fluidization seemed like an ideal operating principle because it ensured heating, prevented compaction, and operated off of feed gas rather than some external power source. Furthermore, the powders to be sprayed were of

the ideal density and size for aeration according to the Geldart powder classification system. (Geldart, 1973)

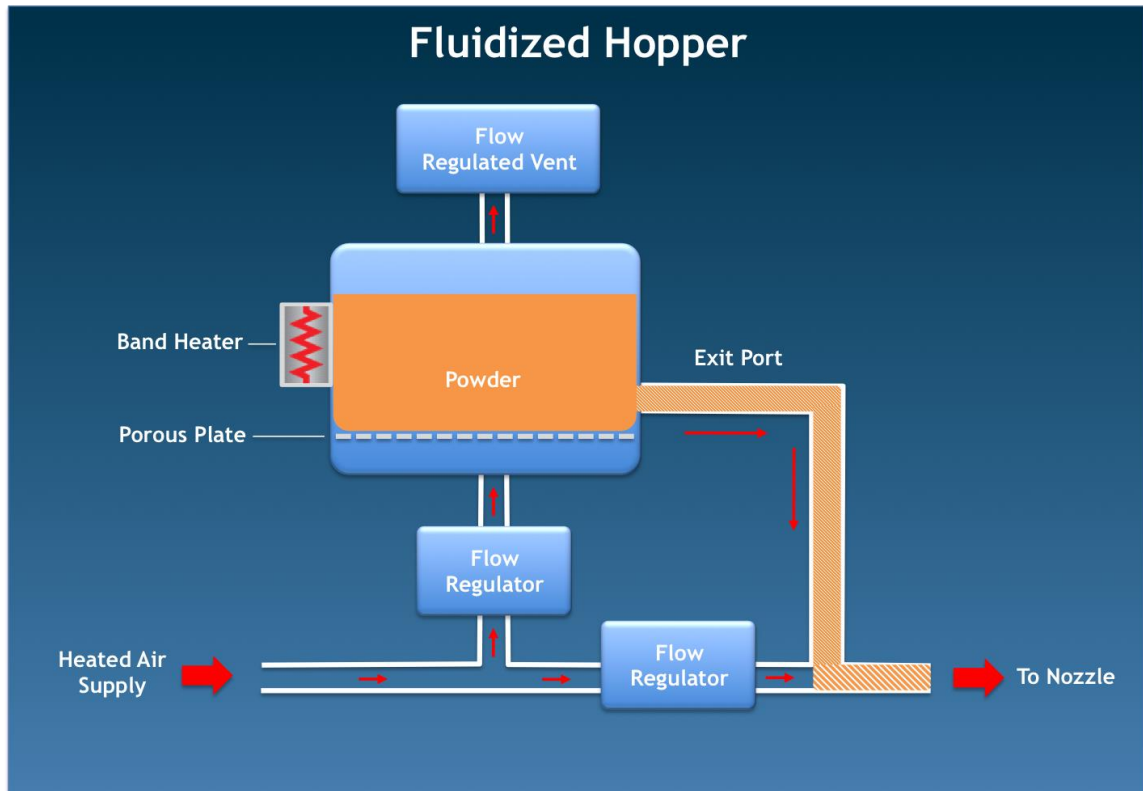


Figure 2-9. Schematic of fluidized powder feed.

The body of the hopper was made from an aluminum pressure vessel with an inner diameter of 33 mm. The porous plate was made from a low density fiberglass filter that was sandwiched between coarse brass mesh for mechanical support. An aluminum ring clamped the filter in place with four screws.

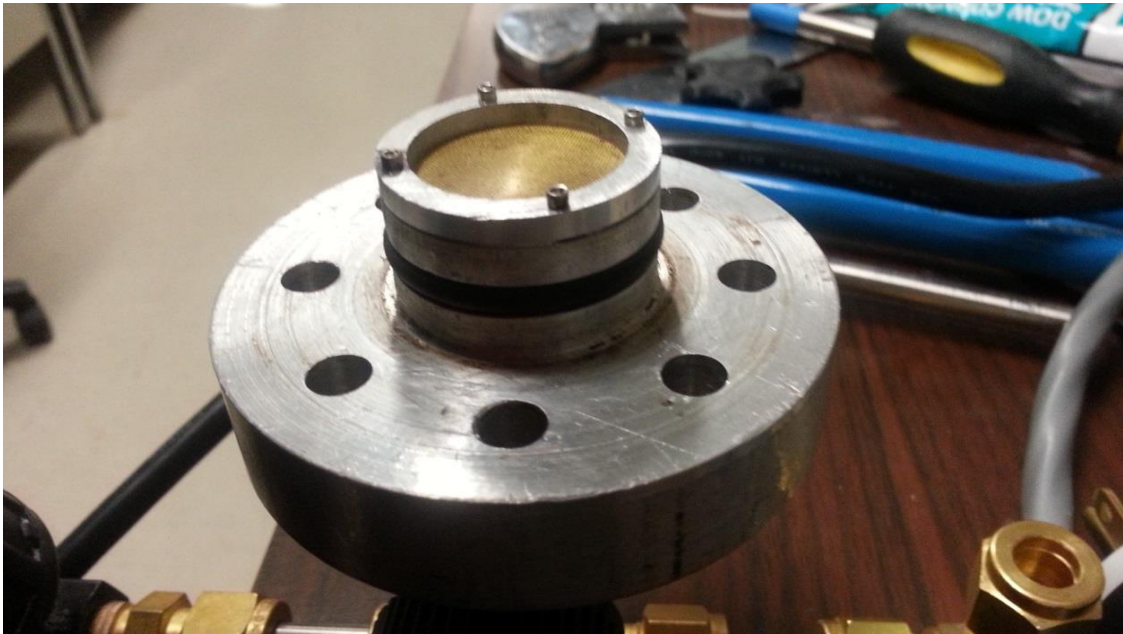


Figure 2-10. Photo of pressure vessel flange with attached porous plate.

Unfortunately, the fluidized hopper design was fraught with difficulties from the outset. The complex gas flow path made powder feed rate difficult to control. Powder feed rate was non-linear with gas flow rate. For polymer powders, high inter-particle forces, especially at high temperature, led to the gas ‘channeling’ through cohesive powder rather than aerating it. This caused intermittency and even cessation of powder flow. Finally, the extra tubing length required by the fluidized system led to a large temperature drop (from 100°C at the heater to 67°C at the nozzle, for example), and some powders even settled out of the gas in the horizontal runs of tubing. A switch to ¼” tube solved the settling problem but at the cost of a 10 psi pressure drop. Because the powder could never exceed its melting

point at any point in the system, there was no way to reach target temperatures at the nozzle with this design.

2.3.3.2 Mechanical Rotating Mesh Hopper

The next attempt at a feed mechanism was a gravity driven, rotating mesh design, inspired by feeders used in commercial cold spray systems. Figure 2-11 shows a schematic overview of this system. A column of powder rested on top of a wire mesh, suspended inside the heated pressure vessel. A shaft ran from a DC motor into the vessel, through the powder column and attached to the wire mesh. The shaft rotated the mesh, agitating the powder and releasing it through the mesh holes. In the first iteration of this design, gas flowed into the vessel, aimed at the underside of the rotating mesh to ensure mixing. The powder/gas mixture then flowed out the bottom of the hopper to the nozzle. Due to gas

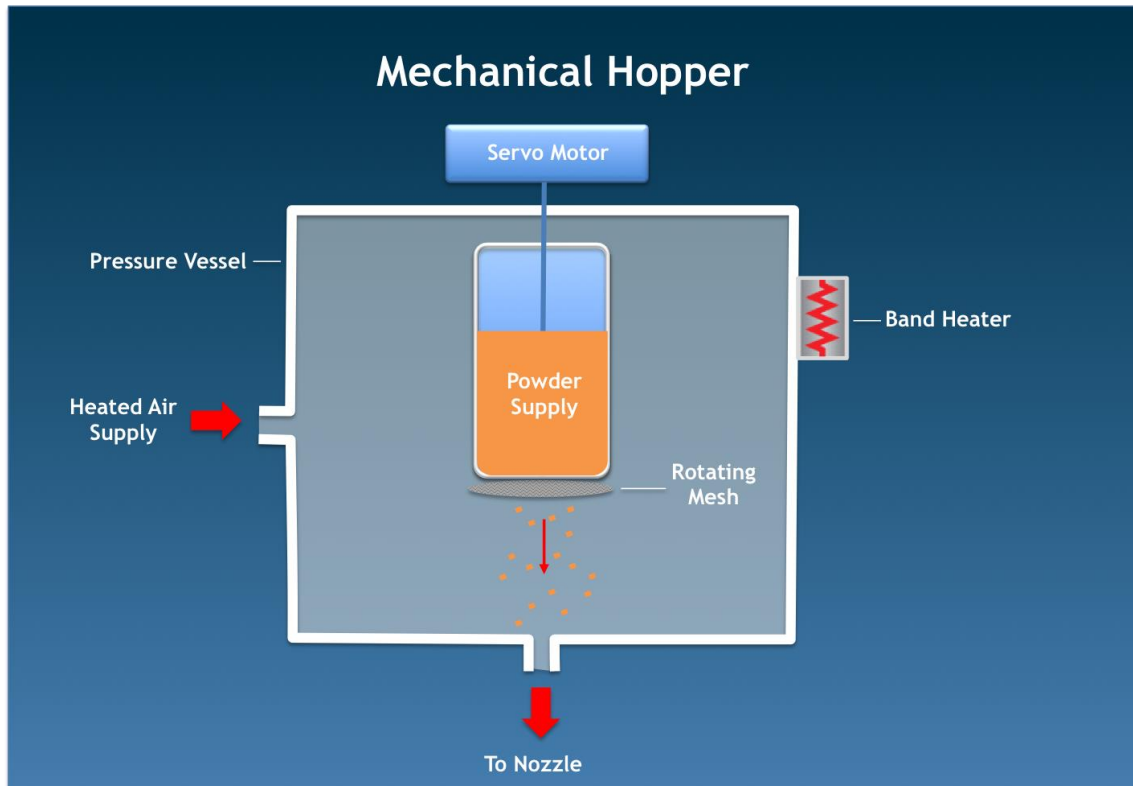


Figure 2-11. Schematic of rotating mesh hopper feed system.

leakage through the shaft fitting, however, powder would float up with the rising gas, contaminate the shaft fittings and interfere with rotation. A modification to fix this problem was to simply flip the pressure vessel over, so that the gas entered at the top of the vessel, flowed over and around the powder and out the bottom. The leakage gas would exit without picking up powder along the way.

This rotating mesh design had several advantages over the previous fluidized bed system. Feed rate was finely controlled by simply increasing the voltage supplied to the DC motor, thus increasing rotation rate. Coarse adjustments in feed rate, such as those necessary when switching powder material, could be made by installing different mesh sizes or by blocking off open mesh area with concentric washers or even aluminum foil. The attractive simplicity of the design and ease of operation made it difficult to admit its shortcomings.

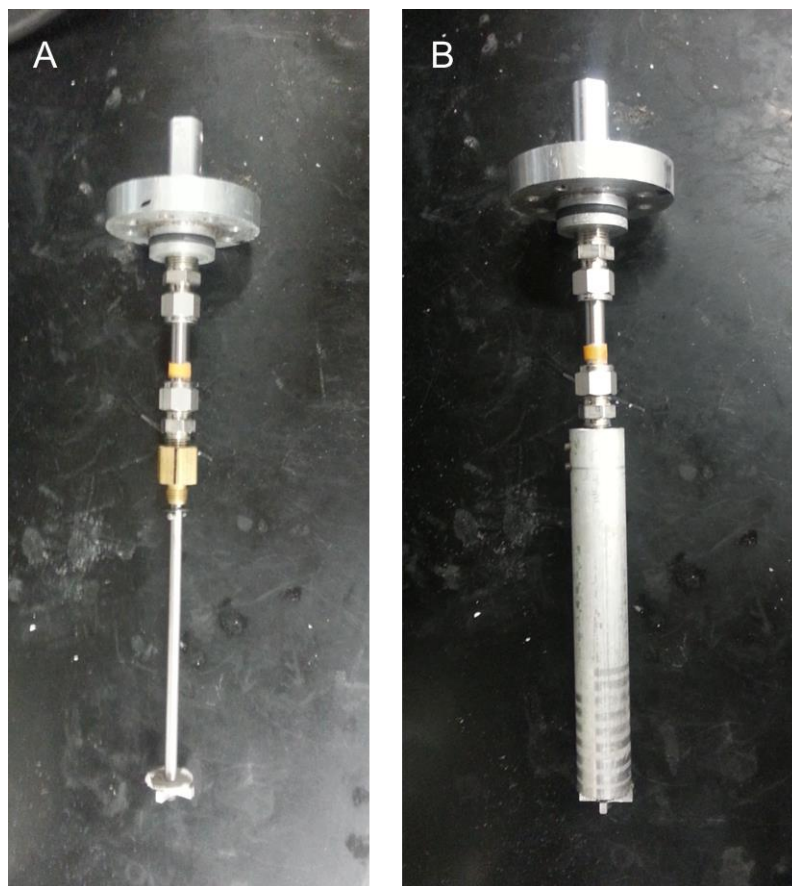


Figure 2-12. Photos of rotating mesh hopper assembly. Shown without (A) and with (B) concentric aluminum hopper insert that contains powder.

The first problem was that the feed rate was dependent on column height. This meant that the feed rate would decline, by a factor of about 2, over the course of a hopper load. The more urgent problem, however, was that the powder feed was not continuous. No matter what steps were taken to limit shaft precession, ensure the hopper sleeve was concentric with the shaft, or ensure the mesh-blocking foil was symmetric, the powder output would pulse once per revolution. At low feed rates, this resulted in evenly spaced dots of deposition seen in Figure 2-13. At higher feed rates, the dots were brought together into an undulating line. This behavior was not conducive to coating production.



Figure 2-13. Photo of 'dots' of deposition resulting from discontinuous powder feed. Sample is BYK Ceraflour 916 sprayed onto LDPE substrate at 25°C and 50 psi.

2.3.3.3 Vibratory Powder Feeder

In an effort to provide a continuous powder feed, the rotating mesh feed mechanism was replaced with a vibrating mesh. At first, the Cleveland Vibrators VM-25 pneumatic vibrator drove, via a connecting rod, oscillation of the mesh on the axis of the gravity fed powder flow. This successfully reduced the time scale of temporal asymmetries to a level that better approximated continuous flow. Instead of pulsing deposition, the vibrating feed mechanism provided a smooth output capable of creating coatings with uniform thickness. The problem with this initial vibratory design was that the powder column would frequently bridge over the vibrating mesh, ceasing deposition.

Eventually, a solution was found for even this final problem: vibrate the entire column. The concentric rod/mesh assembly was removed, and the mesh was attached to the base of the hopper sleeve with epoxy. The sleeve was connected via a shorter connecting rod to the vibrator. In this way, the hopper and mesh vibrated around the contained powder column, ensuring that no binding or sticking could interrupt powder flow.

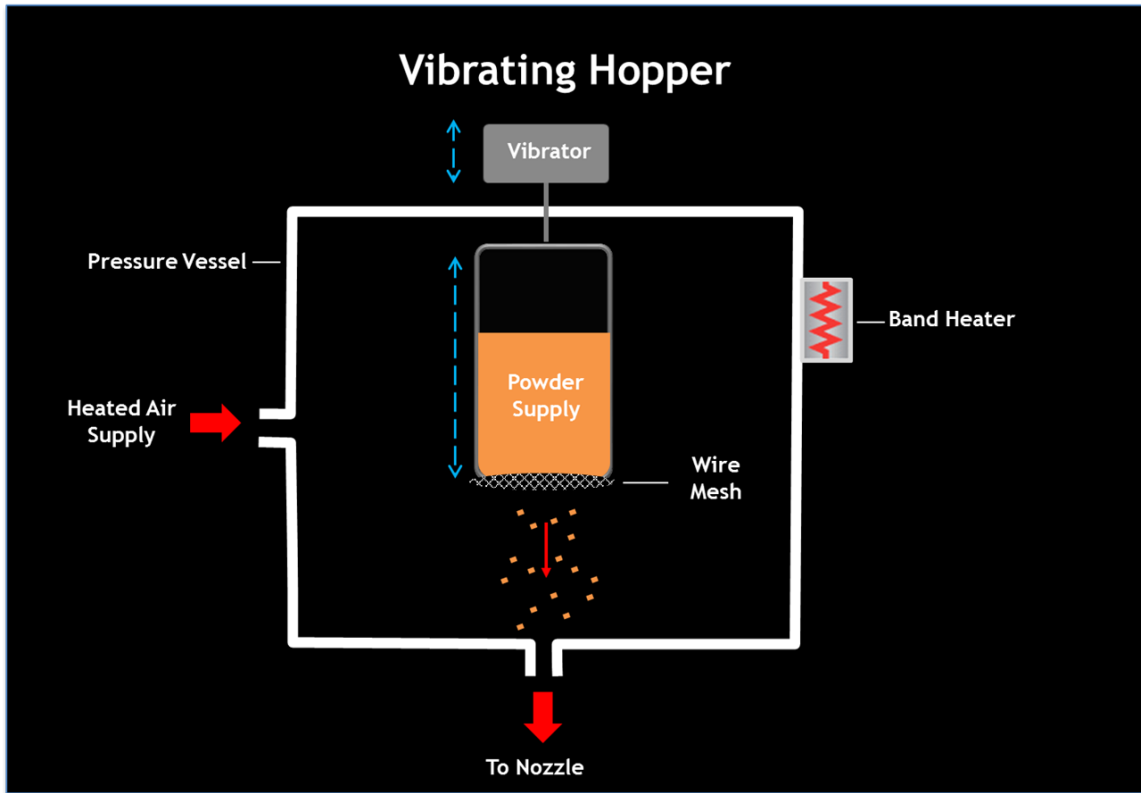


Figure 2-14. Schematic of final vibrating hopper design.

An additional benefit of the vibratory design was a near doubling of hopper capacity. In the rotating mesh design, a considerable portion of hopper volume was occupied by alignment fixtures that attempted to minimize precession of the rotating shaft. The vibratory design does not require such fixtures, and their removal allows that volume to be filled with powder. This nearly two-fold increase of hopper capacity reduced the number of hopper reload processes, which is the principal production bottleneck.

2.3.3.4 Linear Spray System

Testing a powder impregnated with nanoparticles led to a relocation of the spray system into a fume hood. The need for a compact package was also an excuse to redesign the gas routing and eliminate the obsolete parallelism left over from the fluidized bed hopper. The streamlined, linear design can be seen in Figure 2-15. Figure 2-16 shows the actual implementation. An immediate advantage of the compact, vertical design was the return to the wider 3/8" tubing and an overall shortening, which liberated about 15 psi from viscous doom.

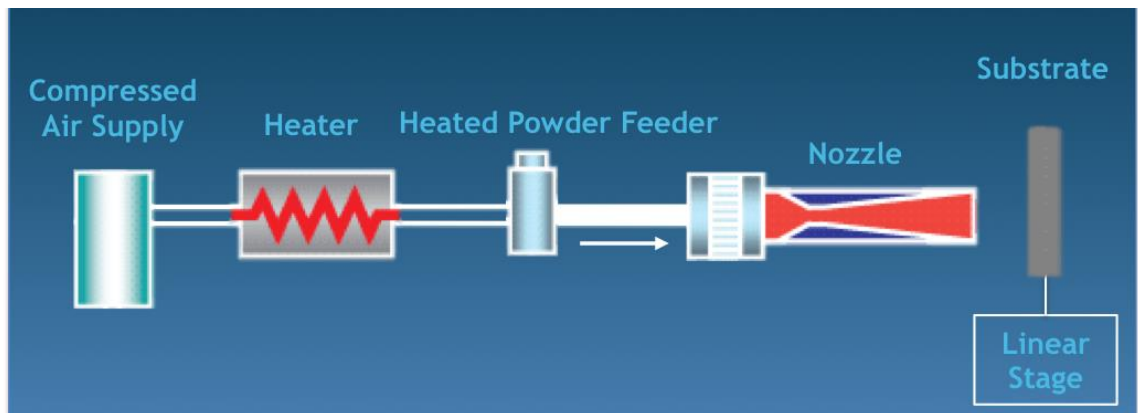


Figure 2-15. Schematic of linear spray system.

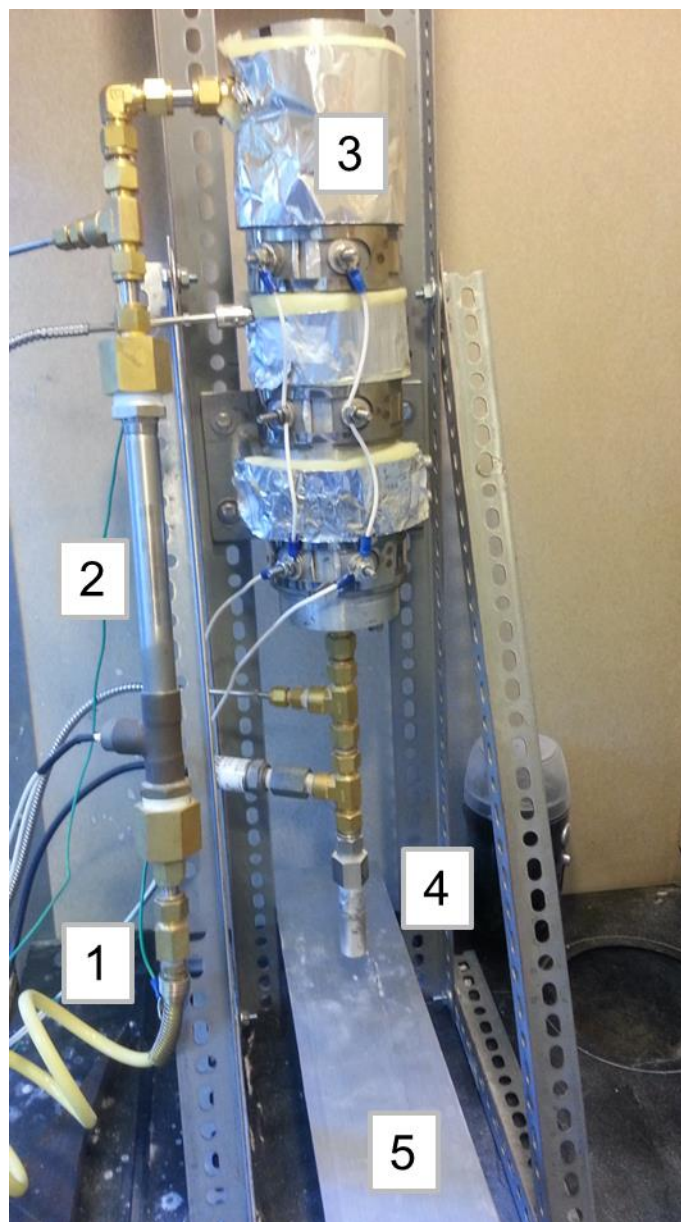


Figure 2-16. Photo of linear spray system. Components are: (1) Gas infeed, (2) Process heater, (3) Heated hopper vessel, (4) Nozzle, and (5) Linear stage.

2.3.4 Material Sourcing

An additional challenge in cold spray of polymers was finding suitable powder sources. Many chemical supply companies and industrial wholesalers supply polymer

powders, but not in the size range necessary for cold spray. Electrostatic spray and rotomolding suppliers typically use much larger particles of at least 150 microns, and more typically 250 microns. Cosmetics suppliers make HDPE microspheres, but only in the 2-9 μm range. Only a single commercial product was found at the proper size: BYK Ceraflour 916. This proprietary product is confusingly termed “HDPE wax” and is marketed as a road paint additive to modify surface texture. The d_{50} (median diameter) is 46 microns, and the d_{90} is 82 microns. DSC peak temperature was 127.8 C, with a lower limit of 124.0 and upper limit of 134.0, per the manufacturer. Additional properties are presented in Table 2-6. It was evident that exploring the material range of polymers required a size reduction capability.

2.3.4.1 Ball Milling

A ball mill was constructed by modifying a consumer-grade rock tumbler. The tumbler operated by resting a mill jar on top of two rollers, one of which was driven by a single-speed motor. Modifications began with half filling the mill jar with 200 1/2-inch diameter chrome steel ball bearings as milling media. Next, the rotation speed at which the milling media were centrifuged against the jar wall (the critical speed) was determined. Ideally, this speed would be given by the force balance in equation 22.

$$\text{Critical Speed} = \frac{1}{2\pi} \sqrt{\frac{g}{R_{jar} - r_{media}}} \quad (22)$$

In practice, however, imperfect momentum transfer between the smooth jar wall and the steel balls meant that this critical speed was too low. A transparent mill jar cap was constructed from PMMA and used to verify the critical condition. Finally, the drive roller diameter was adjusted by wrapping it in layers of gasket material, until the mill jar rotated

at 70% of the critical speed. This rotation rate was chosen on the recommendation of some industrial informational material. (Paul O. Abbe, n.d.) A mechanical Christmas light timer was used to control milling duration.

The ball mill had a capacity of approximately 100g. After a milling session, the powder and media were size separated via a series of wire mesh sieves. The powder sizes produced were: >106 microns, 75-106 microns, 53-75 microns, and <53 microns.

2.3.4.2 Cryomilled Powders

Additional samples were obtained from researchers at KU Leuven via a connection from Professor Jonathan Rothstein. The two thermoplastic polyurethanes and one polyamide were ground to size via a cryomilling process. Commercial cryomilling is typically performed at a scale vastly larger than any research scale project could hope to use. In this case, the researchers at KU Leuven were generous enough to donate some of their oversupply. A full list of materials is seen in Table 2-6.

Table 2-6. Materials and their basic properties. Note: for commercial products, T_g is not given in technical data sheets. The values shown are for generic polymer types.

| Trade Name | Material | T_m ; T_g [°C] | Particle Size [μm] | Flowability |
|----------------------|----------------------------------|--------------------|-----------------------------|-------------|
| BYK Ceraflour 916 | HDPE wax | 135; -90 | 46 | Good |
| Sigma Aldrich HDPE B | HDPE | 112; -100 | Sieved (75-106, 53-75, <53) | Poor |
| Dakotex 8086 | Thermoplastic Polyurethane (TPU) | 148; -20 | Sieved | Poor |
| Unex 4078 | Aromatic TPU | 92; -30 | <80 | Excellent |
| PA 2200 | Polyamide 12 | 185; 130 | 75 | Good |
| Dynoseeds PS40 | Polystyrene | 175; 100 | 40, monodisperse | Excellent |
| | P(BA-EA-MAA) | None; 75 | Sieved | Good |

2.3.4.3 Material Selection

A comprehensive exploration of polymer Cold Spray deposition must encompass a broad range of materials. This study takes the first step toward that long-term goal, and, informed by preliminary explorations of the material range presented above, consists of an in-depth examination of a single material: the commercial product BYK Ceraflour 916. To review, BYK Ceraflour 916 is, according to the manufacturer, a high density polyethylene wax.

To remain consistent with the assumptions behind the working model and behind many FEA studies of cold spray impacts, the LDPE and PMMA substrates from the preliminary work were replaced with substrates of the same material as the deposit: BYK Ceraflour 916. To accomplish this, a base of 6061 aluminum was covered with a layer of melted Ceraflour. To minimize boundary effects from the aluminum base, coating thickness was maintained above a minimum of 250 microns (more than 3 times the d90 particle size of 82 microns, and more than 5 times the d50 size of 46 microns). This substrate thickness is consistent with those found in FEA studies in the literature.

2.4 Experimental Design

The first step in coating characterization is to define the window of deposition. Preliminary experiments have provided some data in the lower range of process capabilities, but a more complete exploration of temperature-pressure space was performed to better define processability. The search for the boundaries of successful deposition was performed as an approximately binary search in pressure at determined temperatures. The pressure search was planned to be performed with a precision of 5 psi, but the surprisingly low critical velocities forced an increase in absolute resolution due to the low pressures

used. 1-D calculations suggested a 5 psi pressure change would produce a 1.0-5.5% change in particle velocity within this experimental domain. This level of precision corresponds to 8.5% of the accessible pressure range of 15-73 psig. But deposition occurred as low as 2 psig, so the maximum resolution of the transducer was used. For reference, recall that maximum pressure resolution is 1 psi. An extra half psi could be estimated based on the oscillation of the pressure reading, but such techniques were used as a last resort.

To compare the data to theory, the conditions of the particle at impact must be known. Directly measuring size, temperature, and velocity of fast-moving, micron-scale particles is difficult in the case of velocity and size, and impossible for temperature. Instead, CFD simulations with a discrete phase model were used to estimate particle conditions at impact. Using numerical results for velocity and temperature, stagnation temperature-pressure space of the carrier gas can be converted to temperature-velocity space of the impacting particles, allowing a direct comparison to the Johnson-Cook critical velocity model.

2.5 Analytical Techniques

2.5.1 SEM

Imaging of both coating surface and cross-section was performed on the FEI Magellan 400 XHR-SEM available in the UMass Polymer Science department. This high-resolution SEM allows nanometer resolution images of adhered particles, both on the surface of the deposit and, via a cross-section cut, on the interface. The low acceleration voltage and low current capabilities of this particular SEM allowed for surface imaging without the use of the conductive gold coatings normally required to image nonconductive

polymers. The drawbacks to this bare-surface imaging were, however, too severe, and gold was sputtered onto the samples.

Porosity was intended to be determined by image analysis of the cross-section using ImageJ software. The built-in particle analysis package accounts for area density of dark (void) and light (deposit) regions of a thresholded binary image. To ensure accurate void identification, analysis was to be performed on three images taken at slightly different angles and the resulting porosity measurements averaged. But SEM imaging revealed no porosity to account for, so image analysis was unnecessary.

Interface resolution of like-on-like deposits, or of chemically similar materials, was problematic due to a lack of contrast between the substrate and deposit as viewed by the SEM. One attempted workaround was to deposit onto Kapton film, which would supposedly provide natural contrast with the polyethylene coating. Deposition was successful, but the bare-surface imaging was impossible due to charge build-up. Once coated with gold, the contrast advantage was moot.

CHAPTER 3

RESULTS AND DISCUSSION

3.1 Preliminary Materials Testing

Four of the six powders obtained were actually sprayed. The milled HDPE and Dakotex TPU powders were so cohesive that they were incompatible with the powder feed systems available at the time. The current vibratory feeder is capable of testing those powders, but the case has not been revisited.

For each material tested, spray conditions were varied from room temperature up to the point that powder ceased to flow from the hopper (about 10-30 degrees below T_m). Of the four materials tested, only BYK Ceraflour successfully deposited on LDPE or acrylic substrates under the aforementioned spray conditions. Each of the three unsuccessful materials exhibited slight erosion, visibly marring the finish of the substrate. In the case of the P(BA-EA-MAA) supplied by Professor Jim Watkins from UMass Polymer Science, the erosion was strong enough to dig trenches in the LDPE and even in the much harder PMMA. As proved by preliminary results, BYK Ceraflour successfully deposited over a broad range of spray parameters, and was therefore chosen as the medium with which to probe the dependence of coating quality upon spray conditions. Table 3-1 shows all negative results.

The spraying process also revealed some unexpected difficulties in powder processing. Powders became tacky and cohesive well below the reported melting point. This was problematic because the nozzles were designed to spray hot, soft particles at lower velocities, but the upper temperature ranges turned out to be beyond reach. The maximum temperature nozzle ended up being unusable except at the highest attainable temperatures.

Table 3-1. Negative results. These conditions produced a visible roughening of substrate surface, but no deposition. Note: BYK did deposit on Kapton film at elevated temperatures of 50 C.

| The following tests used the Max KE nozzle | | | |
|--|-----------|-------------|---------|
| Material | Substrate | T [°C] | P [psi] |
| PS 40 | LDPE | 150 | 0-60 |
| Unex | LDPE | 70 | 0-60 |
| Dakotex | LDPE | never tried | |
| PA 2200 | LDPE | 170 | 0-60 |
| HDPE | LDPE | never tried | |
| P(BA-EA-MAA) | LDPE | 73 | 55 |
| | LDPE | 80 | 65 |
| | LDPE | 85 | 65 |
| | LDPE | 95 | 71 |
| | LDPE | 105 | 71 |
| | LDPE | 49 | 55 |
| | LDPE | 50 | 50 |
| | LDPE | 70 | 75 |
| | LDPE | 50 | 72 |
| | PMMA | 50 | 66 |
| | PMMA | 50 | 66 |
| | PMMA | 70 | 75 |
| BYK | PMMA | 27 | 65 |
| | aluminum | 20-85 | 0-60 |
| The following tests used the Max Temp nozzle | | | |
| BYK | Kapton | 21 | 5 |
| | Kapton | 21 | 10 |
| | Kapton | 21 | 30 |
| | Kapton | 21 | 60 |

3.2 Like-on-Like Deposition of BYK Ceraflour 916

For the first exploration, the same material was used for both powder and substrate. This material homogeneity ensured consistency with modeling assumptions in the critical velocity working model.

3.2.1 Window of Deposition

Figure 3-1 shows the lower boundary of the ‘window of deposition’ for like-on-like deposition of BYK Ceraflour 916. The deposition map is not complete because the upper boundary lies outside of the experimentally accessible domain: the two points with velocities around 260 m/s are the fastest possible spray conditions and produced successful deposits. A higher pressure gas supply is needed to explore the upper erosion boundary.

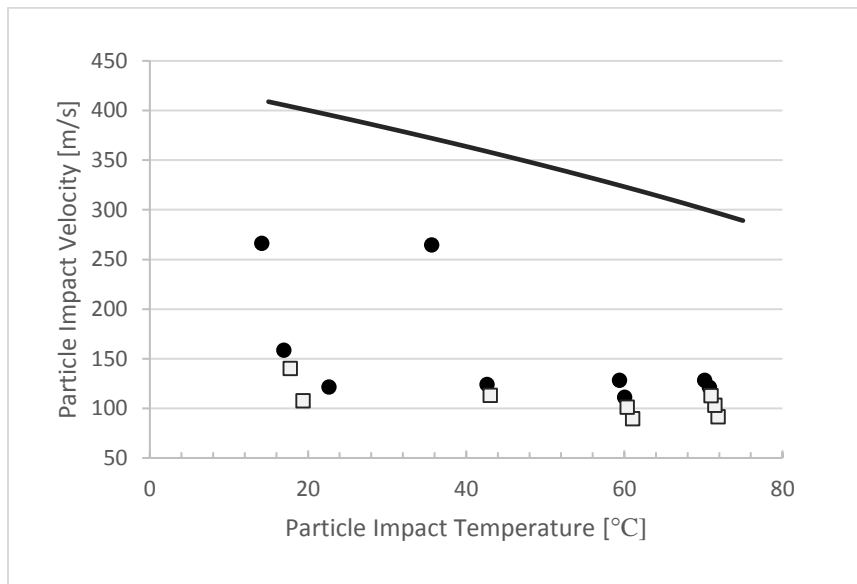


Figure 3-1. Map of lower boundary of deposition for BYK Ceraflour 916 on cast BYK Ceraflour 916 substrate. Filled circles indicate successful deposition, open squares indicate a failure to deposit. The curve is the critical velocity predicted by the working model of Equation 11. (Schmidt, Gärtner, Assadi, & Kreye, 2006)

The obvious observation is how poorly the critical velocity model fits this material. The actual critical velocity is a factor of 3 to 4 less than the predicted value over the entire

range of temperatures. This difference suggests that the degree of plastic deformation or thermal buildup necessary to initiate bonding is much lower for BYK Ceraflour 916 than for metals. This finding is consistent with previous studies of polyolefin deposition. (Xu & Hutchings, 2006) Clearly the mechanics that govern adhesion in metal cold spray differ considerably from the polymer case.

Given the importance of interface temperature in the adiabatic shear instability mechanism, low thermal diffusivity is one possible explanation for the reduced critical velocity seen in polymers. Thermal diffusivity can be 1000 times lower in polymers than metals, so thermal buildup at the interface may be more localized in a polymer. (Swallowe, 1999) Thermal localization means that less total energy needs to be released to attain a given interfacial temperature, thus lowering critical velocity.

3.2.1.1 Measurement Error

Locating the deposition boundary was not always straightforward. Deposition efficiency decays continuously at the boundary, so defining a cutoff point was likely a source of some error. In order to mitigate inconsistency arising from this definitional ambiguity, samples were compared to both previous and contemporary batches when determining what qualified as successful deposition. The numerical deposition boundary was defined as a linear interpolation between the last successful deposit and the first unsuccessful one. A more quantitative approach based on differential mass or image analysis would be strongly preferable, but several barriers stood in the way of such developments:

1. Powder feed was not always well known. Flow rate was a function of vibration intensity, which was a function of pressure supplied to the pneumatic vibrator.

The pressure feeding into the hopper came from the shop air line, which could fluctuate by more than 5 psi. Care was taken before each experiment to adjust the pressure regulator to compensate, but occasionally drift occurred in the middle of a run.

2. Even with consistent flow rate, manual hopper switching meant slight inconsistencies in total powder outflow.
3. Using 'whole hopper' runs to assess efficiency would eliminate powder feed uncertainty, but were prohibitively expensive in terms of powder and, when taking measurements at elevated temperatures, in terms of time as well (due to heating and cooling cycles necessary between runs).
4. 'Powder capacitance' of the system: after cleaning out the hopper, pressure vessel, and tubing (when switching between deposition materials), several grams of the released powder would settle in the corners of fittings and vessels, on the walls of tubing, etc. This could lead to uncertainty in total powder outflow. This was mitigated by dumping bulk powder through the system to saturate it, then tapping out the excess before loading the hopper.
5. Image analysis of deposition spots seems like an attractive solution, but 3-dimensional effects bring its value into question. When descending in pressure, for example, deposits decrease in diameter but increase in height, so total volume is difficult to determine without a stereoscopic setup. Also, lack of contrast between substrate and deposit presents a challenge to the typical thresholding analysis methods.

3.2.2 Structural variation

A deposition map is a useful but incomplete picture of deposition quality because considerable morphological variation occurs as deposition conditions change. Figure 3-2 highlights some of the more dramatic variation in coatings. The lowest velocity sample is smooth but faint, the middle velocity sample is very uniform and robust, and the highest velocity samples display a chaotic and irregular form that even extends, unsupported, out of the plane of the substrate material.

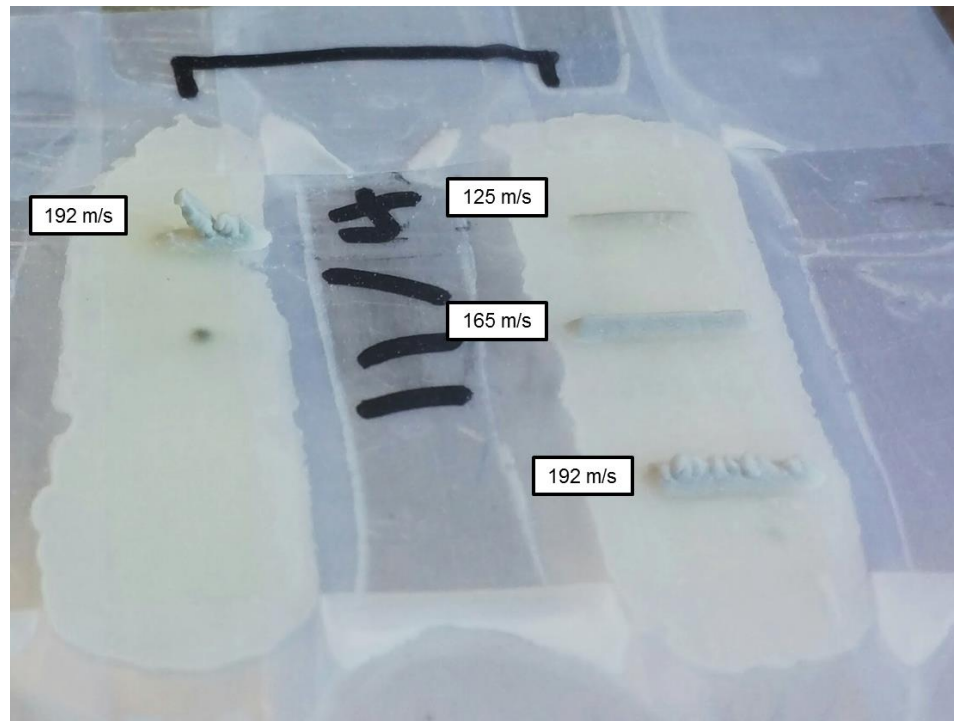


Figure 3-2. Morphological variation in like-on-like BYK Ceraflour deposits sprayed at different velocities. Temperature was constant at 24° C. The nozzle traversed right to left during processing.

Such morphologies encouraged visions of additive manufacturing applications, but raised additional questions concerning not just the mechanics of particle adhesion, but the dynamics of particle flight and impact. It was hypothesized that in the standoff region

between the nozzle exit and the substrate, expansion waves and shock phenomena could interact with particles and lead to variation in impingement angle.

3.2.3 Numerical Simulation of Particle Trajectory

Shock interactions, especially with the bow shock off the substrate, have been shown to negatively impact deposition efficiency. (Pattison, Celotto, Khan, & O'Neill, 2008) We hypothesized that oblique shocks deflected the low-density polymer particles enough to negatively impact deposition efficiency. As I will show, however, numerical simulations suggest that the complex gas dynamics of expansion/compression fans and oblique shocks have only a minor effect on the direction of particle impact. As a worst-case scenario, the shortest (7.21mm) constant-area nozzle was drastically over-pressured with 72psi, generating very strong expansion and compression fans and oblique shocks between the nozzle exit and substrate. At the nozzle exit, the gas accelerates nearly to Mach 3 and turns between +20° and -15° off-axis as it travels through the standoff region.

In order to capture the effects of radial variation in gas velocity, particles were released with an initial radial position r_0 , set in relation to the nozzle exit radius R . The ratio $\frac{r_0}{R}$ ranged from 0.25 to 0.94. The $\frac{r_0}{R} = 0.94$ case is an extreme case in which the particle is released a single particle diameter from the nozzle wall. To avoid modelling the focusing effect of flow through the converging portion of the nozzle, particles were instead released at the nozzle throat, with initial velocities set equal to the previously modeled centerline case. Figure 3-3 shows resulting radial velocity of particles as they traverse the standoff region. As the figure shows, the combination of inertia and brief residence time is such that the 46 μ m particles pick up only a few meters/second of radial velocity (compared to axial velocity of 180-240m/s). Even the most affected particle, released one particle

diameter away from the nozzle wall, was deflected a mere 2.34° off an axis-parallel path over the course of the entire 12.7mm standoff domain. The velocity angle at impact was 6.9° off axis-parallel, alternately stated as an impact impingement angle of 83.1° off of the substrate plane.

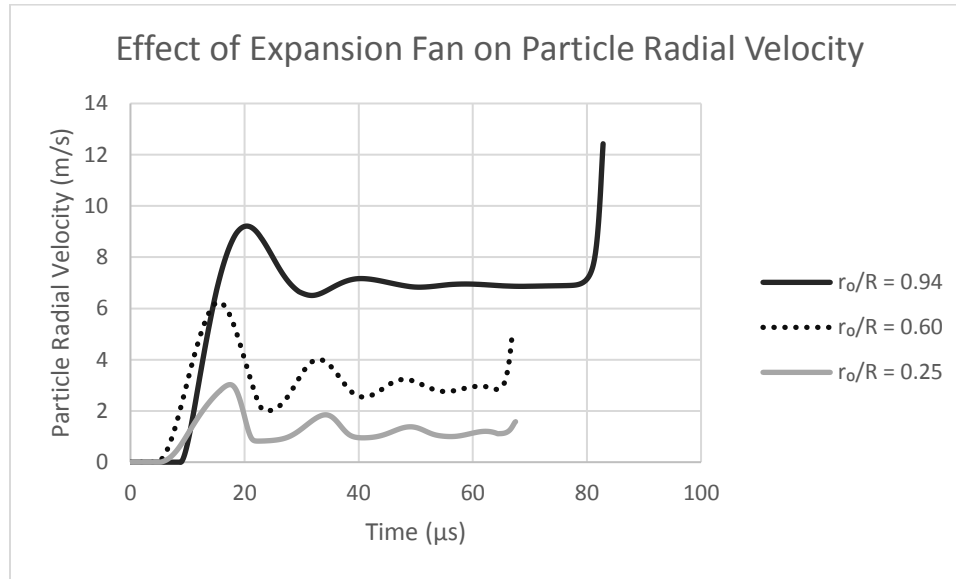


Figure 3-3. HDPE particles ($46\mu\text{m}$ diameter) were released just upstream of the nozzle exit with initial velocities equal to the centerline case. The ratio r_0/R represents the fraction of nozzle exit radius R at which the particles were released. A r_0/R value of 0 corresponds to nozzle centerline, and a value of 1 is the nozzle wall. For reference, particle axial velocity was around 240 m/s for the two most central particles, and 180 m/s for the particle closest to the wall. Inlet gas conditions were $T = 20^\circ\text{C}$, $P = 72\text{ psi}$ in a 7.21mm long constant-area nozzle.

Smaller particles are more effected and achieve higher radial velocity components. A reduction in diameter by factor of 2 results in about a factor of 2 increase in radial velocity, but is also accompanied by an increase in axial velocity (in this case, by about 17%). A $23\mu\text{m}$ particle released at $\frac{r_0}{R} = 0.94$ impacts the substrate at a velocity angle of 11.7° , but if $\frac{r_0}{R} = 0.6$, the angle at impact falls dramatically to 3.5° . While the literature shows that a bow shock reduces deposition efficiency, these worst-case simulations suggest that deflection from oblique shocks is not a likely cause of the lost deposition.

3.2.4 Microscopy

In the hopes that surface topology would provide insight into the adhesion mechanics, an optical microscopy study was conducted. Unfortunately, the available optical techniques lacked sufficient magnification power and struggled for contrast, so an SEM study soon followed. The instrument used was an FEI Magellan 400 XHR-SEM. Figure 3-4 shows some representative samples at different magnification levels. The remarkably featureless topography suggests dense and uniform deposition. A possible explanatory factor to consider while examining surface topography is the low deposition efficiency: more than 95% of particles fail to adhere, and this bombardment of loose particles may be responsible for peening the deposited particles into a dense and smooth deposit. Cross-sectional samples revealed no discernable voids.

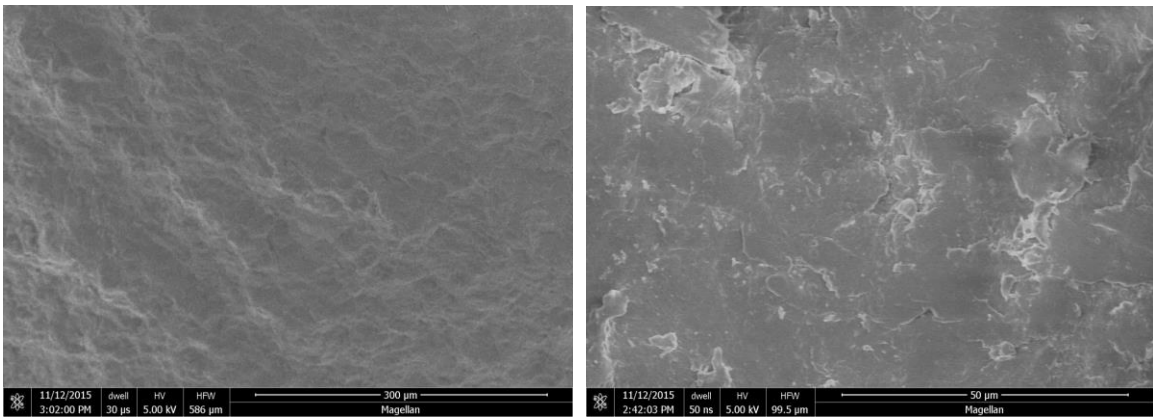


Figure 3-4. SEM imaging of like-on-like BYK Ceraflour deposits. Note the lack of discernable particle boundaries. Deposition conditions at impact: 19° C at 197 m/s (left), 17° C at 228 m/s (right).

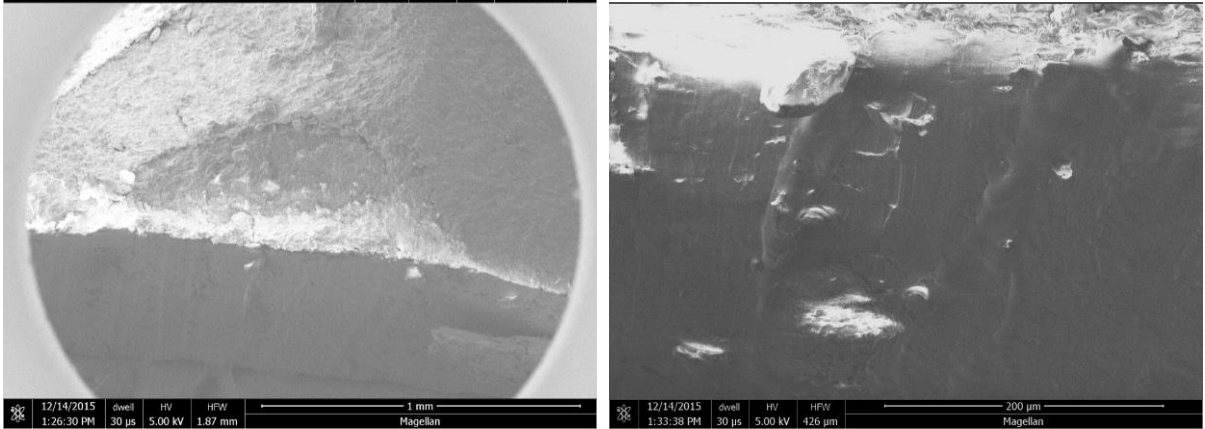


Figure 3-5. SEM of cross section of deposit. A successful deposit was cut in half with a razor blade and the sheared interface imaged with SEM. Left and right images are different zoom levels of the same sample. At impact, a median diameter ($46\mu\text{m}$) particle was 19°C with velocity 179 m/s .

3.3 Variation of Substrate Material

Guided by the critical velocity working model, initial studies of deposition were based around variation in particle impact temperature and velocity. But another variable to tweak is the substrate material. Bae et al. performed a combined FEA and experimental study of metallic deposition and demonstrated that mismatched particle/substrate hardness actually lowers the critical velocity compared to the like-on-like case. (Bae, 2008) When the particle is softer than the substrate, the particle experiences extra plastic deformation, creating a greater contact area and higher temperature compared to the matched case. When the particle is harder, the substrate undergoes the severe deformation. (Bae, 2008) But would this differential hardness effect carry over to polymer deposition? Perhaps choosing an appropriate substrate, and thus lower critical velocities, could lead to higher deposition efficiency.

3.3.1 Windows of Deposition

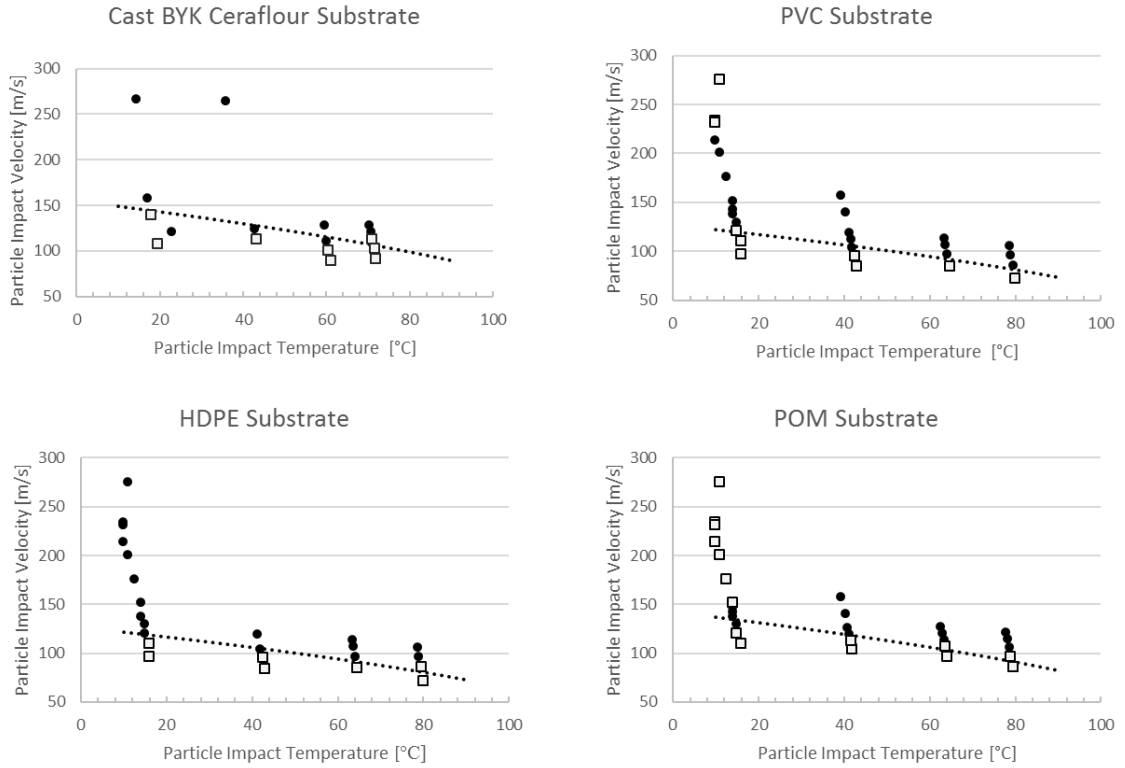


Figure 3-6. Deposition maps of BYK Ceraflour 916 powder on a variety of substrate materials. Closed circles indicate deposition and open squares indicate failure to deposit. The dotted line is a least-squares fit of the working model (equation 11) to the lower deposition boundary (see section 3.3.1.1. ‘Adapting the Critical Velocity Model to Polymeric Deposition’ for details). Boundary points were defined by linear interpolation between the last successful deposit and the first failed deposit points at each temperature. For PVC, POM, and HDPE substrates, room temperature sprays used the converging-diverging to constant-area extension ‘Max Matched-Pressure’ nozzle, and high temperature sprays used the 7.21mm constant area ‘Min velocity’ nozzle. For the cast BYK Ceraflour substrates, the 2 high-velocity points, the 2 points around 40 °C and the low-velocity 22 °C deposit point used the 26.0mm constant-area ‘Max Temperature’ nozzle. All others used the 7.21mm nozzle.

To test the importance of plastic deformation in polymer deposition, four substrate materials were characterized, and the resulting deposition maps are presented in Figure 3-6. The critical velocity was reduced in the mismatched hardness cases, just as

Bae et al. observed. As in the like-on-like case, critical velocity decreases with temperature but is otherwise modeled poorly by the critical velocity model.

Perhaps the most notable difference from the like-on-like case is the appearance of an upper deposition boundary for POM and PVC. In the POM case, the lack of adhesion may not truly indicate an erosion condition. During spraying, a deposit appeared to form, build up, then delaminate from the surface. This process repeated a few times per second. Lower pressure conditions eliminated the delamination effect.

3.3.1.1 Adapting the Critical Velocity Model to Polymeric Deposition

In light of the failure of the metallic deposition model to predict polymer deposition, refitting the empirical constants is a simple first step in evaluating the validity of the functional form and the fundamental physics of the model. With deposition data for a range of substrate materials, the critical velocity model could be empirically fit to each material. Generating separate fitting constants for each substrate case is not particularly useful for producing a predictive model of general polymeric deposition, but these fitting constants are useful as a comparative tool and for quantifying the shift in the deposition boundary for different material combinations.

Returning to the combined equation (equation 10), one step of algebra reveals the functional form. Factor out $(T_m - T_p)$:

$$v_{cr} = \sqrt{\left(F_2 \cdot c_p + F_1 \cdot \frac{4\sigma}{\rho_p} \cdot \frac{1}{T_m - T_{ref}}\right) \cdot (T_m - T_p)} \quad (23)$$

For a given material, the leading term is composed entirely of constants, so the function under the square root is simply linear. So if constants F_1 and F_2 are fit to the same data sample, the thermal, mechanical, and combined models are equivalent. Additionally, this

means the 50% weighting between the constituent models is something of an illusion, because all weighted combinations are equivalent. Because this is a study of a single deposition material, there is no variation in particle material properties that can be used to cross-validate the different models.

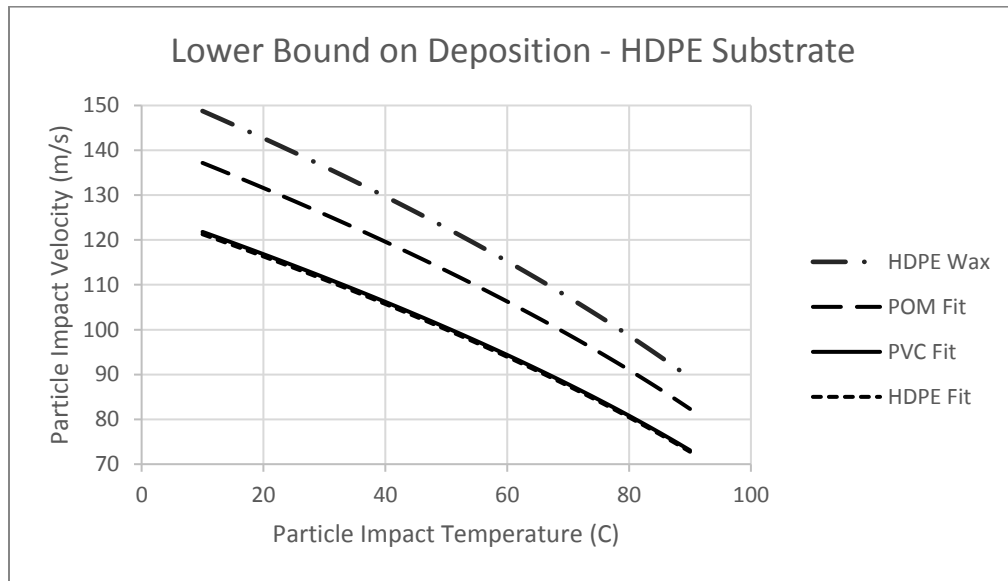


Figure 3-7. Empirical fit of critical velocity model on four different substrates.

Table 3-2. Material and Empirical Fitting Properties. Copper on copper properties are provided for reference. All polymer material properties are from manufacturer data sheets unless otherwise noted.

| Substrate Material | Yield Strength [MPa] | Density [kg/m ³] | Shore D Hardness | Fitting Constant <i>k</i> | R ² |
|--------------------|----------------------|------------------------------|------------------|---------------------------|----------------|
| Cast HDPE Wax | 20 (estimated) | 990 | N/A | 0.187 | 0.62 |
| HDPE | 31.7 | 960 | 69 | 0.152 | 0.67 |
| Acetal (POM) | 65.5 | 1410 | 85 | 0.172 | 0.31 |
| PVC | 88.2 | 1420 | 89 | 0.153 | 0.94 |
| Copper on Copper | 50-85 | 8960 | N/A | 0.548 | N/A |

But even without evaluating the relative validity of the models, comparisons can be made between substrate materials and to the metal case. Figure 3-7 and Table 3-2 illustrate the results of empirical fitting. The form of the critical velocity equation used for fitting is equation 11, reproduced below, in which one fitting constant has been factored out of the radical and the other reduced to a constant.

$$v_{cr} = k \sqrt{c_p(T_m - T_p) + \frac{16\sigma}{\rho_p} \left(\frac{T_m - T_p}{T_m - 293} \right)} \quad (11)$$

The fitting constant for like-on-like deposition of BYK Ceraflour is nearly a factor of 3 less than the copper fitting constant. From an energy perspective (by squaring critical velocity relation, and thus squaring the fitting constant), this implies a reduction by a factor of 9 in energy necessary to produce deposition compared to the case of metals.

Generating separate fitting constants for each substrate case is not particularly useful or desirable for producing a predictive model of general polymeric deposition. These separate fitting constants are, however, useful as a comparative tool, particularly in examining the shift in the deposition boundary with different material combinations.

3.3.1.2 Critical Velocity Comparisons

Just as with metallic deposition, the like-on-like case required the highest critical velocity. (Pattison, Celotto, Khan, & O'Neill, 2008) All other substrate materials tested were harder and had higher yield stress than the deposited material. No obvious relationship was observed between substrate hardness or yield strength and critical velocity. Unfortunately, the lowered critical velocity did not seem to result in any dramatic increase in deposition efficiency.

Returning to the deposition maps of Figure 3-6, we can compare these results to those from the literature. Alhulaifi et al. reported a 191 m/s critical velocity at 120° C impact temperature for 53-76 μm particles of HDPE on 6061 aluminum. The critical velocity of large, room temperature 150 or 250 μm HDPE particles on HDPE substrate was reported as approximately 100 m/s by Xu et al. Without even considering material differences in both deposit and substrate, the present research fits right into the center of the large gap in reported critical velocities in the literature: room temperature, like-on-like deposition of BYK Ceraflour occurred at a critical velocity of 149 m/s.

None of the existing polymer cold spray studies report on the upper erosion boundary of deposition. For metals, the erosion limit is approximated as twice the critical velocity, or a Critical Velocity Ratio (CVR) of 2. (Assadi, et al., 2011). Without a more complete high velocity study, it is perhaps premature to evaluate this condition. But the factor of 2 seems at least plausible based on the limited data available. At room temperature, the test apparatus is not capable of reaching twice the critical velocity for like-on-like deposition. But the highest available velocity, at 1.8 times critical, is successful. At 35° C, the highest velocity is right at CVR = 2, and is again successful. On PVC, all three points above CVR = 1.9 caused erosion, but on LDPE and HDPE, everything was successful, even at CVR of 2.4.

Finally, deposition efficiency has been significantly improved compared to reports from the literature. Xu et al. reported a maximum efficiency of 0.6%. (Xu & Hutchings, 2006) Efficiency measurements in the present study, conducted by Zahra Khalkhali, have produced figures close to 5%, nearly a tenfold improvement. Continued optimization will likely produce further gains in efficiency.

CHAPTER 4

CONCLUSIONS

4.1 Bonding Mechanism

Though critical velocity is lower for polymers compared to metals, deposition efficiency is also reduced. Metallic deposition has benefitted from vastly more research and optimization and there is room for improvement in polymer deposition, but the disparity is stark. Differences in bonding mechanisms likely contribute to this phenomenon.

In cold spray of metals, the formation of metallurgical bonds across the interface is often credited as a potent source of adhesion strength. (Klinkov, Kosarev, & Rein, 2005) Grujicic et al. claim that for metals, adhesion is a nano-length scale process that involves atomic interactions between clean surfaces at high contact pressures. (Grujicic, 2004) But polymeric materials do not generally form such strong chemical bonds.

Polyethylene, being non-polar, is particularly inert, with cohesive strength primarily provided by chain entanglement and overlap, which produce large quantities of weak London dispersion forces. (Yves Gnanou, 2008) In order to produce chain entanglement across an interface, it would seem that either mechanical mixing, melt fusion, or significant diffusion must occur.

The timescale of particle impacts likely rules out a diffusive mechanism. Grujicic et al. calculate that typical metal-metal inter-diffusion distance is between 0.004 and 0.1 nm at temperatures near the melting point and for contact time of 40 ns. Because this distance is only a fraction of inter-atomic distance, they conclude that diffusion should not be considered a dominant mechanism. For HDPE diffusion, the lower thermal diffusivity

and marginally higher inter-diffusion coefficient should lead to greater diffusion distance than for metals. But the distance requirement is also larger than for metals, growing from an angstrom-scale interatomic distance to a nanometer-scale macromolecular radius. Further study may be warranted, but diffusive processes are not likely contributors to adhesion in polymer cold spray.

An additional barrier to chain entanglement is the high crystallinity of HDPE. Chain mobility is inhibited by crystalline formations.

Despite these challenges, there are several possible paths forward. Critical velocity and deposition efficiency may improve with more chemically active or more amorphous polymers. Nylon 66 is an example of a polymer with many hydrogen bonding sites. The bond energy of hydrogen bonds is up to 80 times that of London dispersion forces. (Yves Gnanou, 2008) Ravi et al. have shown that UHMWPE deposition is made possible by the addition of 4 wt.% active filler materials, such as nano-alumina, which form hydrogen bonds between particles. (Ravi, 2015) This enhancement would likely apply to HDPE as well. Another chemical option is a thermally activated cross-linking agent that bridges the particle-particle interface. Finally, particle temperature can be raised by moving the injection point to the nozzle throat. Then high gas temperatures can be used without fear of melting the particles. When used in combination with the extension nozzle or a diffuser nozzle, the post-shock transit of the particles will expose them to the full gas temperature just before impact.

4.2 Summary

The overall goal of this work was to determine the spray conditions that produce successful bonding in a polymeric material. Nozzle geometry, gas parameters, and material

selection were all included in the search space. Substantial development work lead to the creation of an experimental system capable of dispensing, heating, and spraying a polymer powder into a fully dense, uniform, and smooth deposit on a variety of substrate materials. Multiple nozzle geometries were designed and implemented, each optimized for a different region of particle temperature-velocity space. A suitable coating material, BYK Ceraflour 916, was identified despite a relative scarcity of candidate powders.

A systematic experimental regimen probed temperature-pressure space and defined a window of deposition on four substrate materials. Gas temperature-pressure space was transformed to particle temperature-velocity space via CFD simulation, and critical velocities were determined numerically. These critical velocities were validated by existing polymer cold spray literature. Additional CFD work cast doubts on the significance of shock deflection of the relatively low-density polymer powder.

Empirical data also confirmed the phenomenon of depressed critical velocities resulting from mismatched particle/substrate mechanical properties. Deposition efficiency was improved by nearly a factor of 10 from results in the literature. Finally, the industry-standard theoretical framework, designed for metallic deposition, was demonstrated to lack predictive power for polymeric material, and empirical data was used to modify this equation.

BIBLIOGRAPHY

- A. Moridi, S. M.-G. (2014). Cold spray coating: review of material systems and future perspectives. *Surface Engineering*, 369-395 .
- A. P. Alkhimov, V. F. (2001). The features of cold spray nozzle design. *Journal of Thermal Spray Technology*, 375-381.
- Alhulaifi, A. S., Buck, G. A., & Arbegast, W. J. (2012). Numerical and Experimental Investigation of Cold Spray Gas Dynamic Effects for Polymer Coating. *Journal of Thermal Spray Technology*, 852-862.
- Anderson, J. D. (2003). *Modern Compressible Flow, 3rd Edition*. Boston: McGraw Hill.
- ANSYS Academic Research. (n.d.). FLOTRAN Fluids Analysis Guide. In *Release 14.5 Help*.
- ANSYS Academic Research. (n.d.). Fluent Theory Guide. In *Release 14.5 Help*.
- ARL Center for Cold Spray. (2010, 10 13). *Cold Spray Process*. Retrieved 4 1, 2014, from <http://www.arl.army.mil/www/default.cfm?page=370>
- Assadi, H., Gärtner, F., Stoltenhoff, T., & Kreye, H. (2003). Bonding mechanism in cold gas spraying. *Acta Materialia*, 4379–4394.
- Assadi, H., Schmidt, T., Richter, H., Kliemann, J.-O., Binder, K., Gärtner, F., . . . Kreye, H. (2011). On Parameter Selection in Cold Spraying. *Journal of Thermal Spray Technology*, 1161-1176.
- Bae, X. K. (2008). General aspects of interface bonding in kinetic sprayed coatings. *Acta Materialia*, 4858-4868.
- Champagne, V. K. (2011). Theoretical and Experimental Particle Velocity in Cold Spray. *Journal of thermal spray technology*, 20(3).
- Champagne, V. K., & Helfritsch, D. J. (2014). Mainstreaming cold spray – push for applications. *Surface Engineering*, 396-403.
- Ganesan, A., Yamada, M., & Fukumoto, M. (2013). Cold Spray Coating Deposition Mechanism on the Thermoplastic and Thermosetting Polymer Substrates. *Journal of Thermal Spray Technology*, 1275-1282.
- Geldart, D. (1973). Types of Gas Fluidization. *Powder Technology*, 285-292.
- Goharshadi. (2009). Computation of some thermodynamic properties of nitrogen using a new intermolecular potential from molecular dynamics simulation. *Chemical Physics*, 358, 185-195.

- Grujicic, M. Z. (2004). Adiabatic shear instability based mechanism for particles/substrate bonding in the cold-gas dynamic-spray process. *Materials and Design*, 25, 681. doi:10.1016/j.matdes.2004.03.008
- Helfritch, D. (n.d.). General Velocity 13.2 1-D Simulation. Army Research Lab.
- Hussain, T. (2013). Cold Spraying of Titanium: A Review of Bonding Mechanisms, Microstructure and Properties. *Key Engineering Materials*, 533, 53. doi:10.4028/www.scientific.net/KEM.533.53
- Hussain, T. M. (2009). Bonding Mechanisms in Cold Spraying: The Contributions of Metallurgical and Mechanical Components. *J Therm Spray Tech*(18), 364. doi:10.1007/s11666-009-9298-1
- Kaboldy. (2008, 2 10). *De laval Nozzle*. Retrieved 6 6, 2015, from Wikipedia: http://en.wikipedia.org/wiki/De_Laval_nozzle#/media/File:Nozzle_de_Laval_diagram.svg
- Klinkov, S. V., Kosarev, V. F., & Rein, M. (2005). Cold spray deposition: Significance of particle impact phenomena. *Aerospace Science and Technology*, 582–591.
- McCrum, Buckley, & Bucknall. (1997). *Principles of Polymer Engineering*. New York: Oxford University Press.
- Omega Engineering Inc. (2014). *PX309*. Retrieved 3 7, 2014, from How to Order PX309: <http://www.omega.com/pressure/pdf/PX309.pdf>
- Pattison, J., Celotto, S., Khan, A., & O'Neill, W. (2008). Standoff distance and bow shock phenomena in the Cold Spray process. *Surface and Coatings Technology*, 1443–1454.
- Paul O. Abbe. (n.d.). *Mill Speed - Critical Speed*. Retrieved 12 20, 2013, from <http://www.pauloabbe.com/size-reduction/resources/mill-speed-critical-speed>
- Ravi, K. I. (2015). Development of Ultra-High Molecular Weight Polyethylene (UHMWPE) Coating by Cold Spray Technique. *Journal of Thermal Spray Technology*, 24, 1015. doi:10.1007/s11666-015-0276-5
- Schmidt, T., Gärtner, F., Assadi, H., & Kreye, H. (2006). Development of a generalized parameter window for cold spray deposition. *Acta Materialia*, 729–742.
- Swallowe, G. M. (1999). Adiabatic Shear Instability: Theory. In *Mechanical Properties and Testing of Polymers an A-Z Reference* (pp. 15-19). Dordrecht: Springer Netherlands.
- W.-Y. Li, C. Z.-J. (2007). Study on impact fusion at particle interfaces and its effect on coating microstructure in cold spraying. *Appl Surf Sci*, 254, 517. doi:10.1016/j.apsusc.2007.06.026

- W.-Y. Li, C. Z.-T.-J. (2007). Significant influences of metal reactivity and oxide films at particle surfaces on coating microstructure in cold spraying. *Appl Surf Sci*, 253, 3557. doi:10.1016/j.apsusc.2006.07.063
- Walsh, M. (1975). Drag Coefficient Equations for Small Particles in High Speed Flows. *AIAA Journal*, 1526-1528.
- Xu, Y., & Hutchings, I. (2006). Cold spray deposition of thermoplastic powder. *Surface and Coatings Technology*, 3044–3050.
- Yin, S., Zhang, M., Guo, Z., Liao, H., & Wang, X. (2013). Numerical investigations on the effect of total pressure and nozzle divergent length on the flow character and particle impact velocity in cold spraying. *Surface and Coatings Technology*, 290–297.
- Yves Gnanou, M. F. (2008). *Organic and Physical Chemistry of Polymers*. Hoboken, New Jersey: John Wiley & Sons.